ACS OMEGA

Open Access

http://pubs.acs.org/journal/acsodf

Article

Single-Well Simulation for Horizontal Wells in Fractured Gas Condensate Reservoirs

Fuguo Yin,* Shiqing Cheng, Wenpeng Bai, Yang Wang, and Xiuwei Liu

Cite This: *ACS Omega* 2024, 9, 17307−17322

Read Online

ACCESS | Metrics & More | Article Recommendations

ABSTRACT: Fractured gas condensate reservoirs (FGCR) are a complex, special, and highly valuable type of gas reservoir, accounting for a significant proportion of gas reservoir development. In recent years, with the continuous advancement of horizontal well technology, it has become the main approach for the development of FGCR. The current model is unable to accurately represent the fluid distribution in the near-well area of horizontal wells due to the unique retrograde condensation phenomenon in GCR. Additionally, the presence of fractures complicates the solution of traditional analytical models. In response to this issue, this paper proposes a novel semianalytical model for horizontal wells in FGCR, which incorporates natural fractures, multiphase flow, and the influence of stress sensitivity on pressure response. A dual-porosity model is employed to simulate fractured reservoirs, and a four-region radial composite model is developed to characterize multiphase flow resulting from retrograde condensation in GCR. The pseudopressure transform, Pedrosa transform, Laplace transform, and Finite Cosine transform are utilized to address the nonlinear partial differential equation. A systematic verification of the semianalytical solution is confirmed through a comparison with the numerical solution from computer modeling group (CMG). We thoroughly explain the physical significance of the various features by identifying the 12 flow regimes of the typical curve. Furthermore, we offer a method for assessing the extent of retrograde condensation and the size of the retrograde condensate region based on the curve's characteristics. Finally, the pressure measurements recorded from the Bohai field are carried out to validate the accuracy of the proposed model. The results show that the predictions of the new model are in good agreement with the actual production data, demonstrating the proposed solution's applicability.

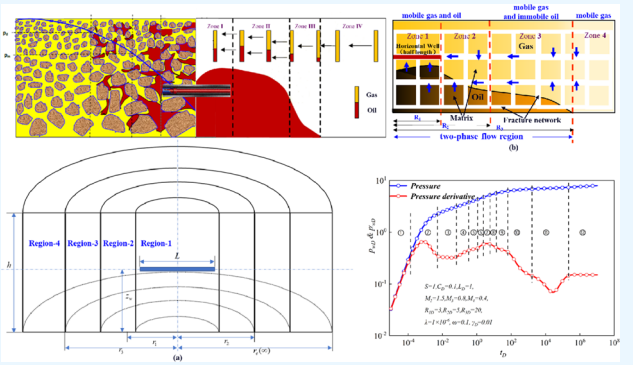

1. INTRODUCTION

Gas condensate reservoirs (GCR) hold a unique and significant position in the world of gas reservoir development. According to statistics, GCR account for 68% of the giant gas reservoirs with geological reserves exceeding 1×10^{12} m^3, and they also make up 58% of the large gas reservoirs with reserves exceeding 1×10^8 m^3.[1,2] GCR are a particular and complex type of gas reservoir with exceptionally high economic value, which has been playing an increasingly significant role in gas reservoir development in the world. As illustrated in Figure 1, during the development of GCR, as pressure decreases, condensate oil tends to precipitate in the vicinity of the wellbore, resulting in a two-phase zone of oil and gas. This phenomenon leads to reduced relative permeability for both gas and liquid phases, ultimately diminishing the production capacity of gas wells.[3,4] In recent years, with continuous improvements in horizontal well technology, it has become a primary means for enhancing production in low-permeability GCR.[5,6] The intricate nature of horizontal well development calls for a systematic approach in monitoring reservoir properties and evaluating the impacts of production measures, highlighting the essentiality of pressure transient analysis (PTA). While PTA techniques for GCR have made significant progress, challenges persist in understanding the flow characteristics for horizontal well, particularly for GCR containing natural fractures.

The study of flow characteristics in horizontal wells originates from research on point source functions. The introduction of point source functions by Gringarten and Ramey marked the inception of their use in the petroleum industry to address unstable reservoir flow.[7] Based on point source function theory, horizontal pressure transient techniques were developed. Daviau was the first to propose an analytical model of horizontal well.[8] Goode introduced another horizontal model, different from Daviau's model in that it assumed reservoir anisotropy ($K_x = K_y$

Received: December 25, 2023
Revised: March 10, 2024
Accepted: March 14, 2024
Published: April 1, 2024

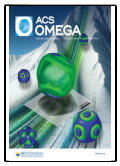

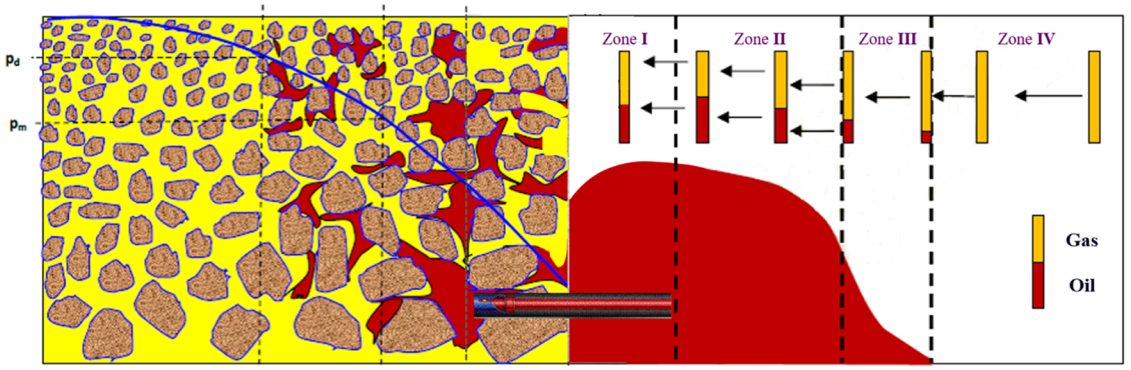

Figure 1. Distribution of formation fluid in horizontal wells used for developing GCR.

= K_z), which adopts the Daviau model while considering the inconsistency of permeability in the horizontal and vertical directions.[9,10] Ozkan utilized the Green function to address the pressure response of horizontal wells in homogeneous and dual-porosity reservoirs with horizontal wells, employing no-flow boundaries above and below, while also considering anisotropic reservoirs.[11−13] Although Green functions and the Newman method had been developed by Gringarten and Ramey in 1973 to solve the problem of horizontal well unstable flow, their practical application has limitations, and it was not until 1991 that Ozkan and Raghavan introduced a comprehensive general solution based on Laplace variables.[14−16] These models and solutions have guided the development and solution of various models of horizontal wells and have provided abundant spatial analytic models for single and corresponding fast calculation methods, greatly enriching theoretical models. Marir studied the horizontal PTA method for dual-porosity sealed oil reservoirs, but there were certain flaws in the pressure response solution, leading to significant errors in later-stage pressure calculations.[17] Hashemi proposed that the superposition principle could be used to consider the effects of wellbore storage and skin factor on pressure response.[18] Baqawi introduced analytical solutions for hydraulic fractured horizontal wells in naturally fractured reservoirs, significantly improving calculation accuracy.[19] Subsequently, pressure transient models of horizontal wells have been continually improved. Cao proposed a transient analysis model for fractured low-permeability gas reservoirs, offering a detailed solution method for transient pressure models in dual-porosity gas reservoirs.[20] These studies offer innovative methods to tackle fluid flow obstacles in fractured gas reservoirs, contributing to the resolution of the nonlinear equations of the FGCR.

Numerous scholars have extensively researched the flow and PTA aspects in GCR. In their studies, Muskat initially introduced the term "condensate blocking" to describe the phenomenon of condensate oil buildup near the wellbore, leading to the creation of a highly saturated zone when the pressure falls below the dew point pressure.[21] This phenomenon results in a reduced relative permeability of the gas phase, leading to diminished production capacity. Jones introduced the concept of multiphase pseudopressures in GCR, subsequently developing various models based on this pseudopressure concept, opening a new era in research on PTA for GCR.[22,23] Following the introduction of the pseudopressure concept, Fevang and Whitson proposed the well-known three-zone flow model for GCR, which later became the most commonly used flow model.[24] Gringarten incorporated the capillary number effect into numerical simulations and discovered that the saturation of condensate oil near the wellbore was not as high as previously thought, but rather lower than in other regions.[25,26] Thus, a four-zone model was introduced to describe the flow characteristics of condensate oil, which was adopted in this study for fluid flow in porous media. Although the GCR model for vertical wells has been gradually improved, the development of the GCR model for horizontal wells is slow. It was not until 2018 that Zhang and colleagues introduced the first composite model for horizontal GCR with three zones, which, however, assumed isotropy and is not applicable to GCR with developed natural fractures.[27] Subsequently, both the vertical well model incorporating natural fractures and the fracturing model for horizontal wells were introduced.[28−30] In recent studies, Wang proposed a novel semianalytical model to accurately describe the bottom-hole pressure behavior of water injectors in fractured reservoirs.[31] Additionally, Wei developed analytical models to comprehensively investigate the intricate thermal behavior of fractured reservoirs.[32] Yin presented a highly sophisticated semianalytical model for GCR, which takes into consideration the intricate effects of multiphase flow, stress sensitivity, and wellbore phase redistribution.[33] However, there is still a dearth of a natural fracture model specifically tailored to the GCR with horizontal wells.

In summary, although numerous studies have focused on single-well simulation in multiphase flow within GCR, relatively little attention has been devoted to studying the combined effects of natural fractures and horizontal wells. Furthermore, the existing model is not precise enough to characterize the retrograde condensation in the near-well region of horizontal wells. Failing to consider the interconnected effects of these factors could result in inaccurate results of single-well simulation and incorrect evaluations of well and formation parameters in FGCR. In this study, we have developed a semianalytical model that takes into account multiphase flow behavior in FGCR. In this paper, a multiregion radial composite model was used to describe the multiphase flow induced by retrograde condensation, while the W-Root model was employed to characterize the fractured reservoir. We also considered the stress-sensitive variation of fracture permeability with changing pressure. To solve the model, Laplace transformation, Pedrosa transformation, and Cosine transformation are applied to convert the partial differential equations into ordinary differential equations. A numerical simulation model was established using commercial software (CMG),[34] and the results were found to be highly consistent with the model proposed in this paper, thereby validating the correctness of our model. The solutions obtained from the model can be displayed as type curves, which effectively illustrate the impact of retrograde

https://doi.org/10.1021/acsomega.3c10360
ACS Omega 2024, 9, 17307−17322

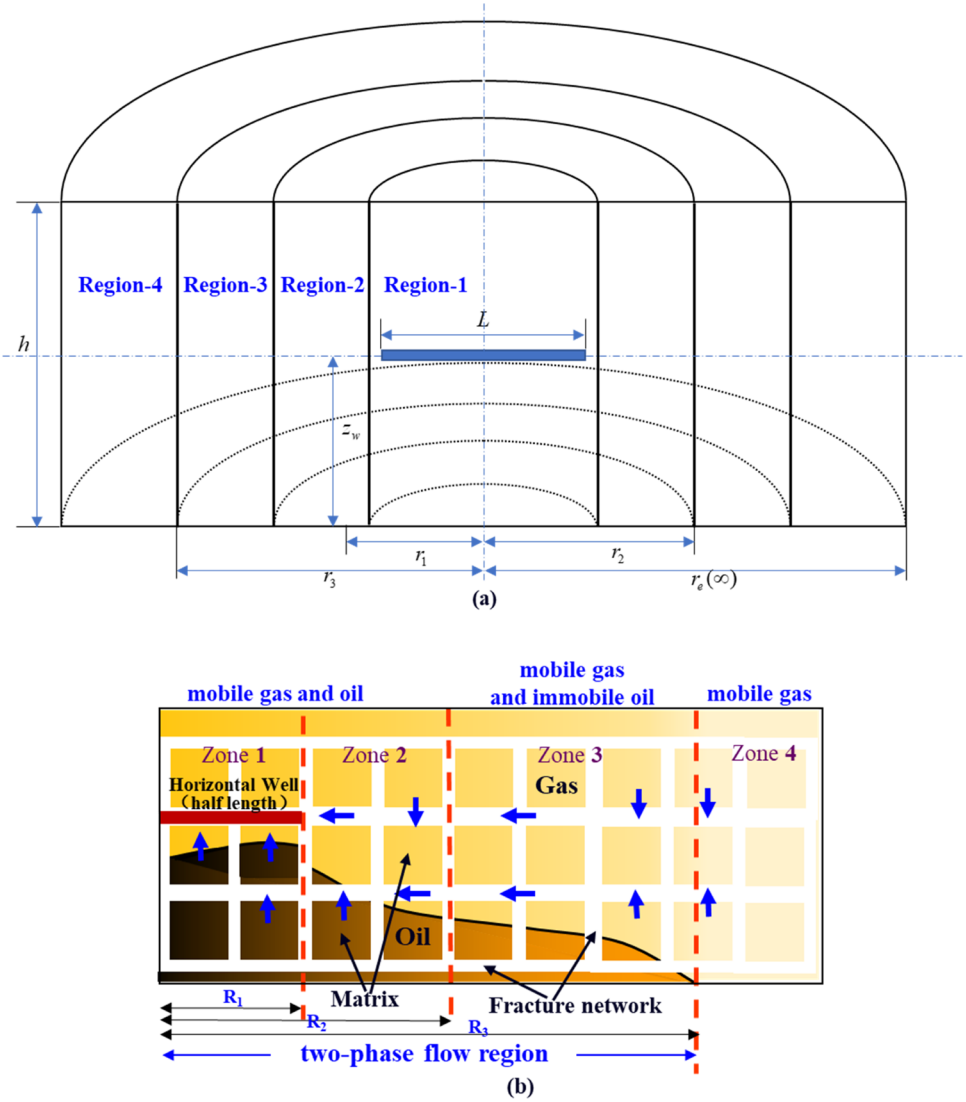

Figure 2. Model of FGCR based on the dual-porosity model: (a) physical model, (b) flow model.

condensation and natural fractures. Ultimately, the proposed model was successfully utilized to interpret a field case in the Bozhong field.

2. METHODOLOGY

2.1. Physical Model. During the development of the GCR, there will be several distinct flow regions in the formation as the pressure decreases. The composite models are consistently used to simulate the well production process, where the reservoir is clearly divided into multiple zones with different properties. Experiments show that four flow zones with different fluid saturation can be observed around the horizontal well in GCR due to retrograde condensation.[35] Figure 2 shows the physical model.

(1) Region-1: the gas and condensate oil are mobile, and condensate saturation reaches critical saturation. In addition, the oil saturation in region-1 is lower than that in region-2 because some of the oil is carried away as a result of the high speed of gas flow and the high capillary number.[36]

(2) Region-2: the oil and gas are mobile and the condensate saturation is higher than region-1.

(3) Region-3: oil and gas coexist in region-3, but only gas is mobile because the oil saturation in this region is below the critical flow saturation.

(4) Region-4: in this region, retrograde condensation does not take place and only gas is mobile.

To establish the mathematical model, certain assumptions are made as follows:

(a) The gas condensate reservoir is a homogeneous infinite reservoir with dual porosity, characterized by a consistent thickness.

(b) The fluid flow within the reservoir is isothermal and follows Darcy's law.

(c) The pressure remains continuous at the interfaces between different regions.

(d) The horizontal well is completely located in region-1.

(e) The initial pressure is higher than the dew point pressure.

(f) The upper and lower parts of the reservoir are impermeable.

2.2. Analytical Model. The permeability of fractures varies as a function of pressure, and its relationship with pressure is as follows:

https://doi.org/10.1021/acsomega.3c10360
ACS Omega 2024, 9, 17307−17322

$$\gamma = \frac{1}{K_f}\frac{\partial K_f}{\partial p} \tag{1}$$

Based on the characteristics of the aforementioned four-zone model, we derive the flow equations used to describe the production of horizontal wells in GCR according to the W-R model.[37] For zone-1 ($i = 1$) and zone-2 ($i = 2$), we obtain

$$\begin{cases} \frac{1}{r}\frac{\partial}{\partial r}\left[K_{ifh} r\left(\frac{K_{rfo}\rho_o}{\mu_o} + \frac{K_{rfg}\rho_g}{\mu_g}\right)e^{-\gamma(p_r - p)}\frac{\partial p}{\partial r}\right] \\ \quad + \frac{\partial}{\partial z}\left[rK_{ifv}\left(\frac{K_{rfo}\rho_o}{\mu_o} + \frac{K_{rfg}\rho_g}{\mu_g}\right)e^{-\gamma(p_r - p)}\frac{\partial p}{\partial r}\right] \\ \quad = \phi_f\frac{\partial(S_{fo}\rho_o + S_{fg}\rho_g)}{\partial t} - F_s K_{im}\left(\frac{K_{rmo}\rho_o}{\mu_o} + \frac{K_{rmg}\rho_g}{\mu_g}\right) \\ \quad (p_m - p_f) \\ F_s K_{im}\left(\frac{K_{rmo}\rho_o}{\mu_o} + \frac{K_{rmg}\rho_g}{\mu_g}\right)(p_m - p_f) \\ \quad + \phi_m\frac{\partial(S_{mo}\rho_o + S_{mg}\rho_g)}{\partial t} = 0 \end{cases} \tag{2}$$

For zone-3, the flow equations can be written as

$$\begin{cases} \frac{1}{r}\frac{\partial}{\partial r}\left[K_{3fh} r\left(\frac{K_{rfg}\rho_g}{\mu_g}\right)e^{-\gamma(p_r - p)}\frac{\partial p}{\partial r}\right] \\ \quad + \frac{\partial}{\partial z}\left[rK_{3fv}\left(\frac{K_{rfg}\rho_g}{\mu_g}\right)e^{-\gamma(p_r - p)}\frac{\partial p}{\partial r}\right] \\ \quad = F_s K_{3m}\left(\frac{K_{rmg}\rho_g}{\mu_g}\right)(p_m - p_f) + \phi_f\frac{\partial(S_{fg}\rho_g)}{\partial t} \\ F_s K_{3m}\left(\frac{K_{rmg}\rho_g}{\mu_g}\right)(p_m - p_f) + \phi_m\frac{\partial(S_{mg}\rho_g)}{\partial t} = 0 \end{cases} \tag{3}$$

For zone-4, the following flow equations are obtained:

$$\begin{cases} \frac{1}{r}\frac{\partial}{\partial r}\left[K_{4fh} r\left(\frac{K_{rfg}(S_{wi})\rho_g}{\mu_g}\right)e^{-\gamma(p_r - p)}\frac{\partial p}{\partial r}\right] \\ \quad + \frac{\partial}{\partial z}\left[rK_{4fv}\left(\frac{K_{rfg}(S_{wi})\rho_g}{\mu_g}\right)e^{-\gamma(p_r - p)}\frac{\partial p}{\partial z}\right] \\ \quad = F_s K_{4m}\left(\frac{K_{rmg}(S_{wi})\rho_g}{\mu_g}\right)(p_m - p_f) + \phi_f\frac{\partial(S_{gfi}\rho_g)}{\partial t} \\ F_s K_{4m}\left(\frac{K_{rmg}\rho_g}{\mu_g}\right)(p_m - p_f) + \phi_m\frac{\partial(S_{mgi}\rho_g)}{\partial t} = 0 \end{cases} \tag{4}$$

The partial differential equation described above is seriously nonlinearized. The two-phase pseudopressure is used to solve this problem. In this research, we utilized the method suggested by Fevang and Whitson to compute the two-phase pseudopressure.[24]

The pseudopressure for zone-1 ($i = 1$) and zone-2 ($i = 2$) can be represented as

$$\begin{cases} m_{if}(p) = \int_{p_{wf}}^{p^*}\left(\frac{K_{rfo}}{\mu_o}\rho_o + \frac{K_{rfg}}{\mu_g}\rho_g\right)dp \\ m_{im}(p) = \int_{p_{wf}}^{p^*}\left(\frac{K_{rmo}}{\mu_o}\rho_o + \frac{K_{rmg}}{\mu_g}\rho_g\right)dp \end{cases} \tag{5}$$

For zone-3 these are given by

$$\begin{cases} m_{3f}(p) = \int_{p^*}^{p^d}\left(\frac{K_{rfg}}{\mu_g}\rho_g\right)dp \\ m_{3m} = \int_{p^*}^{p^d}\left(\frac{K_{rmg}}{\mu_g}\rho_g\right)dp \end{cases} \tag{6}$$

For zone-4, we obtain

$$\begin{cases} m_{4f} = K_{rfg}(S_{gi})\int_{p^d}^{p}\left(\frac{\rho_g}{\mu_g}\right)dp \\ m_{4m} = K_{rmg}(S_{gi})\int_{p^d}^{p}\left(\frac{\rho_g}{\mu_g}\right)dp \end{cases} \tag{7}$$

The flow equation for each region ($i = 1, 2, 3, 4$) can be linearized based on the aforementioned pseudopressure:

$$\begin{cases} \frac{1}{r}\frac{\partial}{\partial r}\left[r\frac{\partial m_{if}}{\partial r}\right] + \gamma\left(\frac{\partial m_{if}}{\partial r}\right)^2 + \frac{K_{ifv}}{K_{ifh}}\left[\frac{\partial^2 m_f}{\partial z^2} + \gamma\left(\frac{\partial m_{if}}{\partial r}\right)^2\right] \\ \quad = e^{-\gamma(m_r - m)}\left[\frac{1}{\xi_{if}}\frac{\partial m_{if}}{\partial t} + \frac{1}{\xi_{im}}\frac{\partial m_{im}}{\partial t}\right] \\ F_s K_{im}(m_{im} - m_{if}) + \frac{K_{ifh}}{\xi_{im}}\frac{\partial(m_{im})}{\partial t} = 0 \end{cases} \tag{8}$$

A comprehensive derivation of the linearization procedure is provided in Appendix A.

The dimensionless equations for the four zones ($i = 1, 2, 3, 4$) can be derived by utilizing the dimensionless variables defined in Appendix B. The resulting dimensionless mathematical model is presented below:

$$\begin{cases} \frac{1}{r_D}\frac{\partial}{\partial r_D}\left(r_D\frac{\partial m_{ifD}}{\partial r_D}\right) + \gamma_D\left(\frac{\partial m_{ifD}}{\partial r_D}\right)^2 + L_D^2 \\ \quad \left[\frac{\partial^2 m_{ifD}}{\partial z_D^2} + \gamma_D\left(\frac{\partial m_{ifD}}{\partial z_D}\right)^2\right] = (h_D L_D)^2 e^{-\gamma m_{ifD}} \\ \quad \left[(1 - \omega)\frac{\partial m_{imD}}{\partial t_D} + M_i\omega\frac{\partial m_{ifD}}{\partial t_D}\right] \\ (1 - \omega)\frac{\partial m_{imD}}{\partial t_D} = -\lambda(m_{imD} - m_{ifD}) \end{cases} \tag{9}$$

The connection condition is that the pressure and fluid velocity are identical at the common boundary.

https://doi.org/10.1021/acsomega.3c10360
ACS Omega 2024, 9, 17307−17322

$$\begin{cases} m_{1fD}(r_{D1}, t_D) = m_{2fD}(r_{D1}, t_D) \\ \left.\dfrac{\partial m_{1fD}}{\partial r_D}\right|_{r_D=r_{D1}} = \dfrac{1}{M_2}\left.\dfrac{\partial m_{2fD}}{\partial r_D}\right|_{r_D=r_{D1}} \\ m_{2fD}(r_{D2}, t_D) = m_{3fD}(r_{D2}, t_D) \\ \left.\dfrac{\partial m_{2fD}}{\partial r_D}\right|_{r_D=r_{D2}} = \dfrac{M_2}{M_3}\left.\dfrac{\partial m_{3fD}}{\partial r_D}\right|_{r_D=r_{D2}} \\ m_{3fD}(r_{D3}, t_D) = m_{4fD}(r_{D3}, t_D) \\ \left.\dfrac{\partial m_{3fD}}{\partial r_D}\right|_{r_D=r_{D3}} = \dfrac{M_3}{M_4}\left.\dfrac{\partial m_{4fD}}{\partial r_D}\right|_{r_D=r_{D3}} \end{cases} \tag{10}$$

The outer boundary condition (infinite reservoir) is given by

$$p_{4fD}(\infty, t_D) = p_{4mD}(\infty, t_D) = 0 \tag{11}$$

The inner boundary condition can be expressed as

$$\begin{cases} \lim\limits_{\varepsilon_D \to 0}\left[\lim\limits_{r_D \to 0}\int_{z_{wD}-\varepsilon_D/2}^{z_{wD}+\varepsilon_D/2}\left(r_D e^{-\gamma_D p_{1fD}}\dfrac{\partial p_{1fD}}{\partial r_D}\right)dz_{wD}\right] = \dfrac{1}{2} \\ |z_D - z_{wD}| \le \dfrac{\varepsilon_D}{2} \end{cases} \tag{12}$$

The initial condition is given as

$$p_{ifD}(r_D, 0) = p_{imD}(r_D, 0) = 0, \quad i = 1, 2, 3, 4 \tag{13}$$

2.3. Model Solution. To derive a point source solution for a horizontal well, the first step is to eliminate the nonlinearity of the equation by applying the Pedrosa variable substitution. Next, the Laplace transform is utilized on the time variable, and orthogonal transformation is performed on the spatial variable, converting the differential equation into a standard Bessel equation and obtaining the point source solution. Finally, the point source solution is integrated to calculate the horizontal well pressure response, resulting in the expression of the bottom-hole pressure response in the Laplace domain (the detailed derivation of the model solution is presented in Appendix C). The Laplace domain solution can be obtained for the horizontal well pressure:

$$\begin{aligned} \overline{\eta}_{wDN} = & \int_{-1}^{1}\frac{1}{2u}[K_0(r_D\sqrt{F_1^0(u)}) + gI_0(r_D\sqrt{F_1^0(u)})]dz_{wD} \\ & + \int_{-1}^{1}\sum_{1}^{\infty}\frac{\cos(n\pi z_D)\cos(n\pi z_{wD})}{u}[K_0(r_D\sqrt{F_1^n(u)}) \\ & + gI_0(r_D\sqrt{F_1^n(u)})]dz_{wD} \end{aligned} \tag{14}$$

where $r_D = \sqrt{(x_D - x_{wD})^2 + (y_D - y_{wD})^2}$.

An expression can be obtained that takes into account the reservoir effect and skin effect by using the Duhamel principle:[38]

$$\overline{\eta}_{wD} = \frac{u\overline{\eta}_{wDN} + S}{u + C_D u^2(s\overline{\eta}_{wDN} + S)} \tag{15}$$

The dimensionless pseudopressure η_{wD} can be determined by converting the Laplace domain outcome in eq 16 to the real domain via the utilization of the Stehfest numerical inversion method.[39] Finally, the Pedrosa transformation is used to solve the solution considering the effect of stress sensitivity.

$$\Psi_{wD} = -\frac{1}{\gamma_D}\ln(1 - \gamma_D\eta_{wD}) \tag{16}$$

3. VALIDATION AND LIMITATION

To validate the accuracy of the semianalytical model, a numerical model is constructed using the commercial simulator CMG, with the same parameters set up for comparison with the model proposed in this paper. Table 1 provides a comprehensive breakdown of the reservoir and fluid properties.

Table 1. Properties of FGCR and Fluid

parameters	value
original pressure, MPa	55
porosity, %	20
horizontal well length, m,	400
dew point pressure, MPa	48
max liquid dropout,%	24.86
horizontal permeability, 10^{-3} μm^2	50
vertical permeability, 10^{-3} μm^2	5
critical oil saturation,%	10
reservoir outer radius, m	2000

Figure 3 displays the constant volume depletion (CVD) test curve. Figure 4 illustrates a comparison between the outcomes

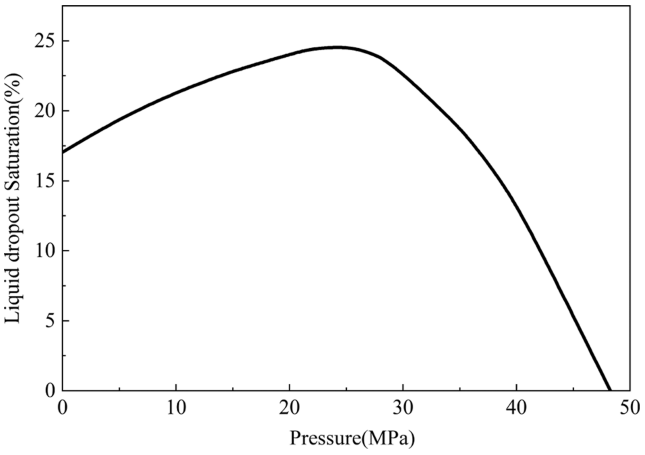

Figure 3. CVD curve.

obtained from the commercial simulator and the proposed model. The remarkable consistency observed between the proposed model and the commercial simulator serves as a testament to the dependability and precision of the proposed model.

4. RESULTS AND DISCUSSION

4.1. Type Curves. Figure 5 depicts the PTA-type curve of a horizontal well in FGCR. Based on the shape characteristics of the type curve, each flow regime of the curve is determined.

Regime 1: Wellbore storage regime. The pressure and its derivative curves exhibit unit slope characteristic.

Regime 2: The skin effect regime. The presence of a hump in the pressure derivative is attributed to the skin effect, indicating the onset of fluid flow from the reservoir into the wellbore.

Regime 3: Early vertical radial flow regime. The third regime is the early vertical radial flow regime, where the pressure derivative curve approximates a horizontal line and its value is

https://doi.org/10.1021/acsomega.3c10360
ACS Omega 2024, 9, 17307−17322

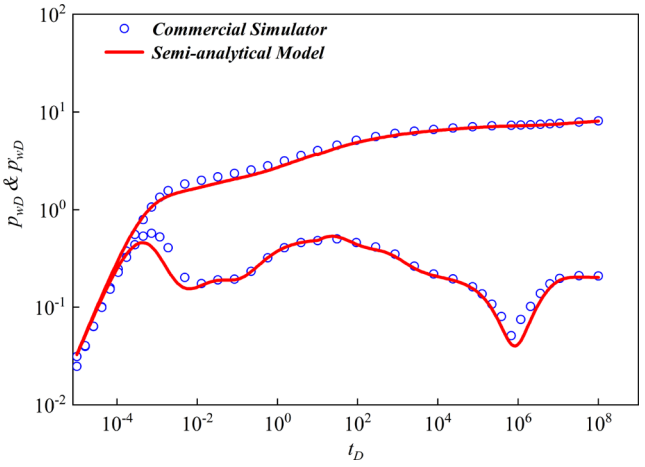

Figure 4. Comparison of results obtained from commercial simulator and proposed model.

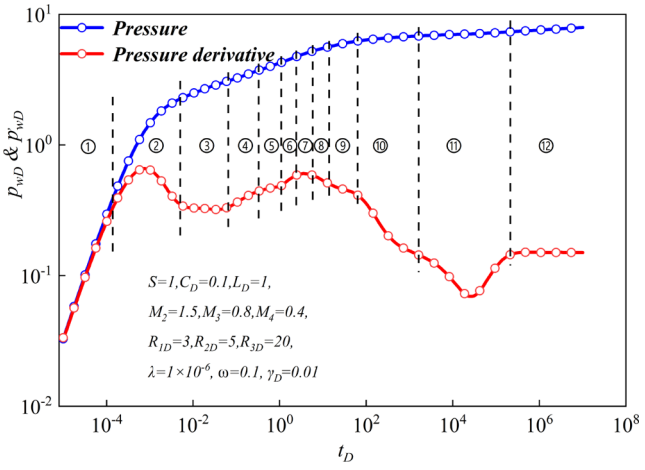

Figure 5. Type curve of FGCR

associated with "L_D". In horizontal wells with relatively high wellbore storage coefficients, the early vertical radial flow stage may be obscured by the impact of wellbore storage.

Regime 4: Horizontal well linear flow regime. The pressure derivative curve is a straight line with a slope of 0.5 in this stage, indicating the propagation of pressure waves to the boundary, resulting in a linear flow perpendicular to the horizontal well.

Regime 5: The zone-1 radial flow regime. The pressure derivative curve is a horizontal line with a value that remains around 0.5, indicating the influence of the capillary number on the oil-gas two-phase flow.

Regime 6: The zone-1 transitional flow regime. The derivative curve exhibits an upward trend, indicating the propagation of pressure waves from zone-1 to zone-2.

Regime 7: The zone-2 radial flow regime. The derivative curve undergoes a transition to a new horizontal line with a value of 0.5 × M_2, which represents the oil-gas two-phase flow that is independent of the capillary number.

Regime 8: The zone-2 transitional flow regime. The pressure derivative curve exhibits a downward trend, indicating that the pressure wave is spreading from zone-2 to zone-3.

Regime 9: The zone-3 radial flow regime. The pressure derivative horizontal line of 0.5 × M_2 × M_3 represents the gas phase flow in the condensate blockage area.

Regime 10: The zone-3 transitional flow regime. This trend continues as the pressure wave spreads from zone-3 to zone-4, with the drop in the pressure derivative, suggesting high fluidity in zone-4.

Regime 11: Interporosity regime. Due to the flow from the matrix to the natural fractures, the derivative curve takes on a V-shape.

Regime 12: The zone-4 radial flow regime. This indicates the initial state of the FGCR, in which the pressure derivative exhibits a horizontal line with a value of 0.5 × M_2 × M_3 × M_4.

During the radial flow regime, the pressure derivative curve exhibits an initial rise, followed by a decline, indicating varying mobility across different zones. However, the presence of these flow regimes is dependent on factors such as wellbore storage and well and reservoir dimensions, as revealed in the sensitivity analysis.

4.2. Sensitivity Analysis. The pressure of horizontal well in FGCR is anticipated to be influenced by the factors listed below: permeability modulus, composite radius, wellbore storage coefficient, interporosity flow coefficient, and mobility ratio. The impact of the aforementioned parameters on the pressure was examined using the model presented in this paper.

4.2.1. Wellbore Storage Coefficient C_D. The impact of different wellbore storage coefficients (C_D = 0.01, 0.05, and 0.1) on transient pressure behavior was analyzed while keeping other parameters constant, as illustrated in Figure 6. The pressure and

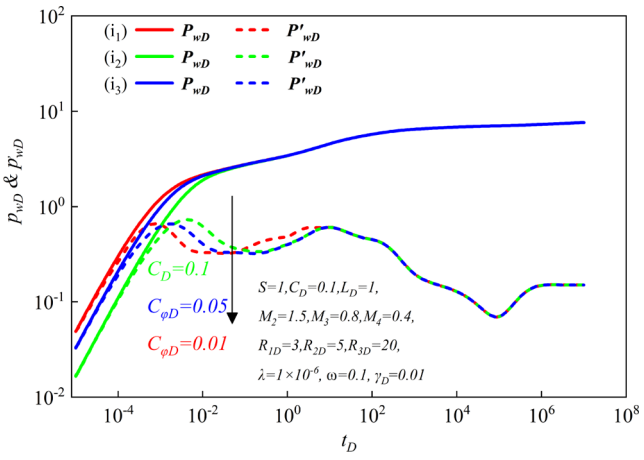

Figure 6. Impact of the dimensionless wellbore storage coefficient (C_D) on type curves

derivative curves both exhibit a slope of 1. A smaller C_D value results in an earlier appearance of the derivative curve's "hump". As the C_D value increases, the curve shifts to the right, obscuring the characteristics of early vertical radial flow. Additionally, when the radius of the first zone is small, the radial flow characteristics of this zone may not be readily apparent. Nevertheless, this does not affect the pressure behavior beyond the second transient flow regime.

4.2.2. Permeability Modulus γ_D. Figure 7 illustrates the variations in dimensionless pressure for different permeability modulus (0.1, 0.03, and 0.01). It is apparent that the pressure response is affected by the permeability modulus except during the wellbore storage regimes. The pressure derivative curve exhibits an upturned characteristic in the later stages due to stress sensitivity. Overall, both the pressure and its derivative curve tend to increase as the permeability modulus rises. Significantly, the upturned characteristic of the pressure

https://doi.org/10.1021/acsomega.3c10360
ACS Omega 2024, 9, 17307−17322

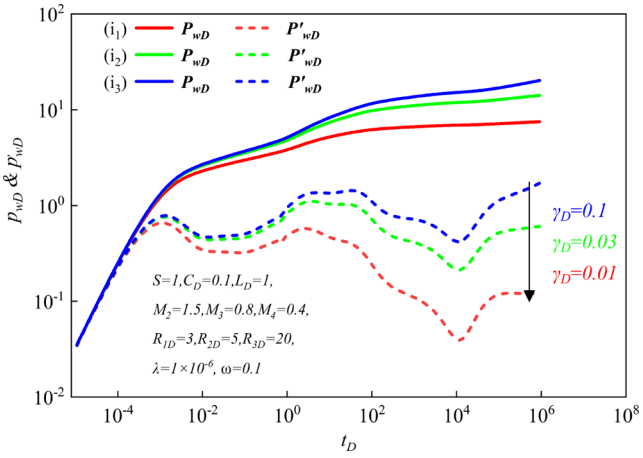

Figure 7. Impact of permeability modulus (γD) on type curves.

derivative curve in the later stages can also be linked to a closed boundary. Therefore, it is imperative to exercise additional caution when observing an upward shift of the pressure derivative curve in the later stages, since it could be an outcome of stress sensitivity rather than a closed boundary.

4.2.3. Composite Radius R_{jD}. Figure 8 illustrates the pressure and its derivative characteristics under examination of three distinct composite radius (R_{1D}, R_{2D}, R_{3D}). R_{1D} is varied as 1, 2, and 3, while R_{2D} and R_{3D} remain constant, as depicted in Figure 8a. It is evident that an increase in the radius value of zone-1 leads to an extended duration of the zone-1 radial flow regime while making the characteristics of the zone-1 transition regime and the zone-2 radial flow regime less pronounced. The type curves for other zones exhibit a pattern similar to that of zone-1. As a result, it becomes viable to define the boundaries of the retrograde condensate region through an analysis of the radial flow phase regimes.

Furthermore, when summarizing the observations from Figure 8a−c, it becomes apparent that when the radii between two adjacent zones are about the same size, identifying the four-zone feature on the type curve can be challenging. This suggests that even if retrograde condensation takes place within the formation, it may not be easily distinguishable from the pressure test curve when the condensate bank is small. Therefore, there are scenarios where it becomes imperative to assess the degree of condensate blockage by conducting multiple pressure measurements.

4.2.4. Interporosity Flow Coefficient λ. We have considered three different scenarios of the interporosity flow coefficient, denoted as λ ($\lambda = 1 \times 10^{-5}$, 5×10^{-5}, 1×10^{-6}). In Figure 9, it is evident that the type curves exhibit significant overlap, except within the interporosity regime. Notably, the "V-shape" phenomenon shifts to the left as the interporosity flow coefficient increases. In simpler terms, a higher value of the interporosity flow coefficient leads to an earlier appearance of the "V-shape". This phenomenon is primarily attributed to the interporosity flow coefficient's influence on the interporosity regime. A larger interporosity flow coefficient facilitates fluid movement between the matrix and fracture, resulting in the interporosity regime occurring at an earlier stage. It is essential to highlight that as the interporosity flow coefficient diminishes, the "V-shape" materializes within the domain of the radial flow regimes. For instance, when the interporosity flow coefficient equals 1×10^{-5}, the "V-shape" emerges in the region associated with zone-3 and obscures the characteristics of the zone-3 radial

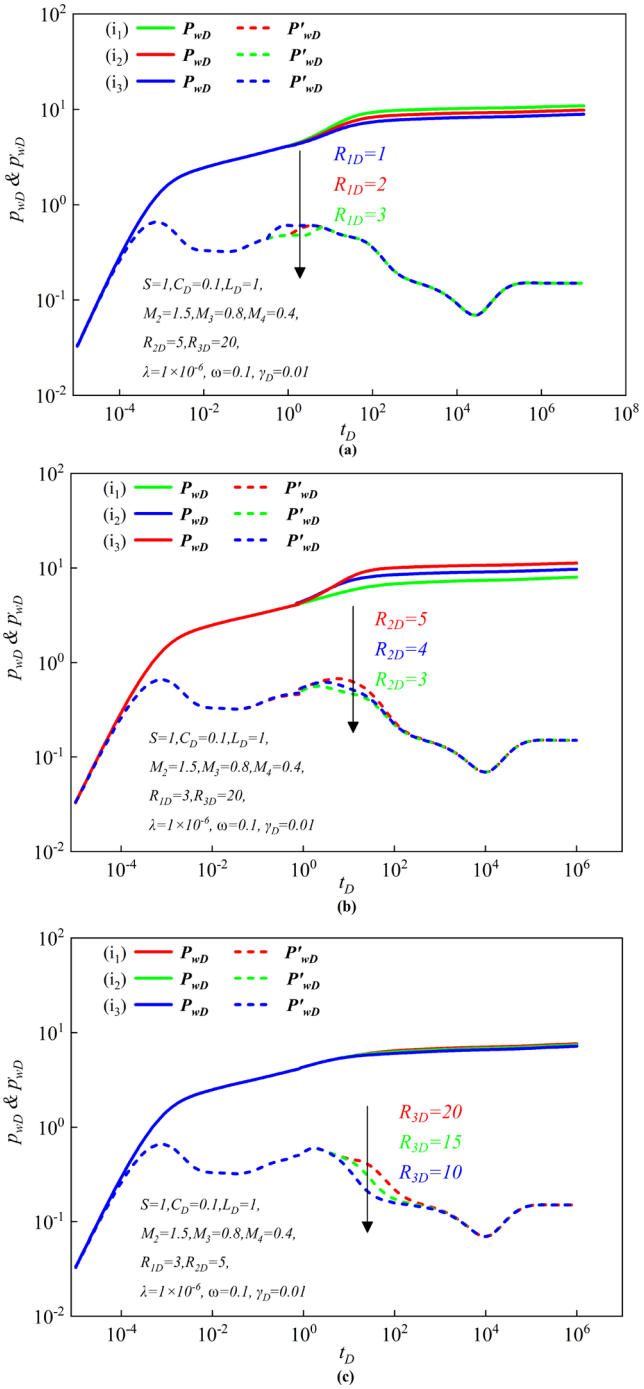

Figure 8. Impact of composite radius (R_{jD}) on type curves: (a) R_{1D}, (b) R_{2D}, (c) R_{3D}.

flow regime. It indicates that more extensive development of fractures within the reservoir results in a postponement of the onset of the interporosity regime.

4.2.5. Storativity Ratio ω. The impact of different two-phase storativity ratios (ω = 0.03, 0.05, and 0.1) is illustrated in Figure 10. It is evident from the results that, except for the interporosity regime, pressure and its derivatives exhibit substantial overlap across these three cases. As the ω value increases, the storage capacity of fractures gradually diminishes. Simultaneously, the depth of the V-shaped pressure curve becomes shallower, and the onset of the interporosity regime is delayed with increasing ω. This phenomenon can be attributed to the fact that in

https://doi.org/10.1021/acsomega.3c10360
ACS Omega 2024, 9, 17307−17322

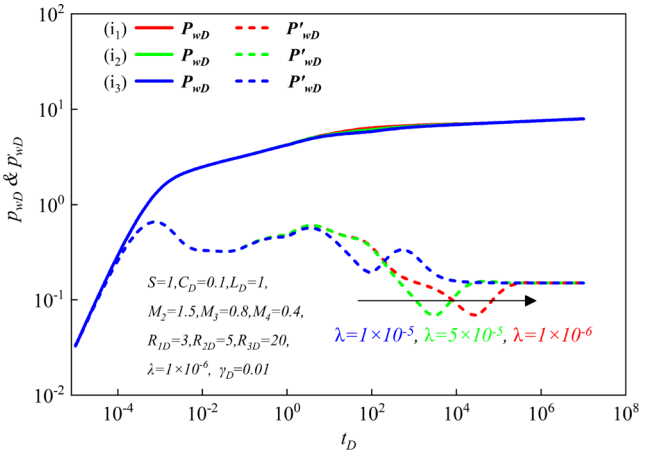

Figure 9. Impact of the interporosity flow coefficient (λ) on type curves.

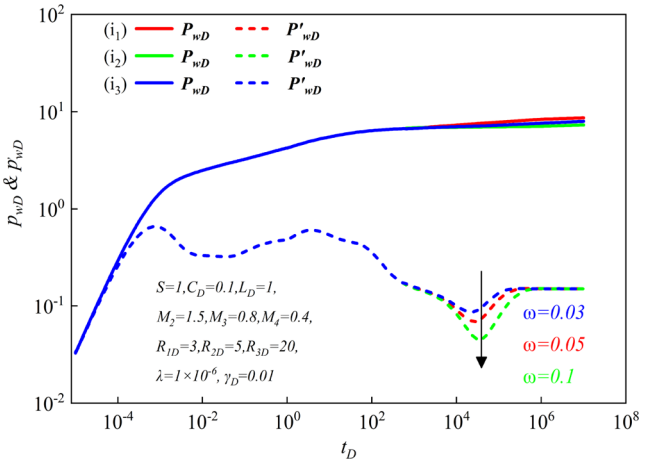

Figure 10. Impact of storativity ratio (ω) on type curves.

formations with larger fractures, fluid within the fracture system initially escapes when the formation pressure declines. In other words, it takes more time to observe a noticeable pressure differential between the matrix and fracture when the fractures are extensive. Fluid from the matrix only begins to migrate toward the fractures once a significant pressure drop occurs. Consequently, in formations with more extensive fractures characterized by a higher number of fractures, larger openings, and enhanced connectivity, the interporosity regime commences at a later stage.

4.2.6. Mobility Ratio M_i. The impact of the mobility ratio is illustrated in Figure 11. The mobility ratio exerts a minimal impact on the pressure curve, while the pressure derivative curve exhibits greater sensitivity to this parameter. To further analyze this effect, we focus on Zone-2 as demonstrated in Figure 11a. In this case, three different mobility ratios for Zone-2, denoted as M_2 (M_2 = 1.1, 1.2, 1.5), are selected. It becomes apparent that, with the exception of the second radial flow regime and the second transitional flow regime, the pressure and its derivative curve overlap across these three cases. Notably, the pressure and its derivative curve display an upward trend after the first radial flow regime as M_2 increases. Moreover, the pressure derivative curve demonstrates that as M_2 decreases gradually, the characteristics of the second radial flow regime become less distinguishable, resulting in a pressure transient response that more closely resembles that of a three-zone system. Moreover,

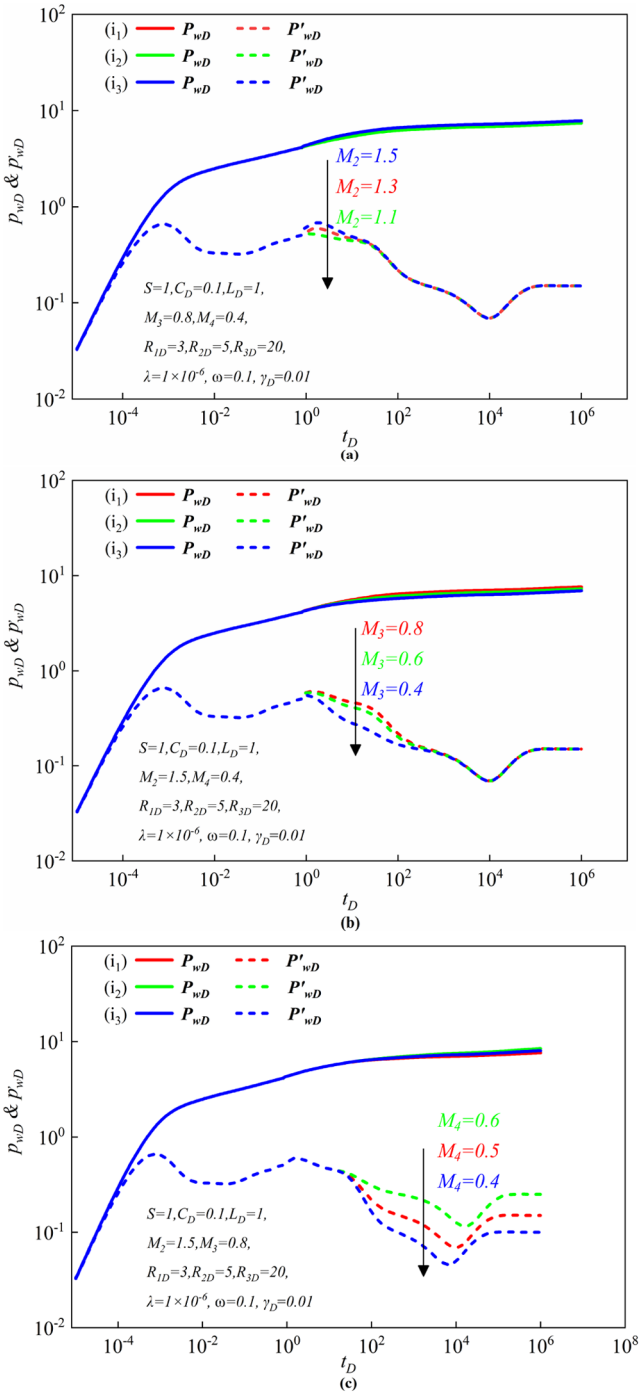

Figure 11. Impact of mobility ratio (M_i) on type curves: (a) M_2, (b) M_3, (c) M_4.

the influence of the mobility ratio on the derivative curve is uniform across different zones, as illustrated in Figure 11b,c.

5. CASE STUDY

Y Buried Hill gas condensate reservoir was discovered in recent years in China with a maximum liquid dropout of 24.6% at 26 MPa and a dew point pressure of 48.73 MPa. The seismic detection shows that fractures are developed in the reservoir. The experimental results demonstrate that the gas condensate reservoir exhibits low-permeability characteristics. A typical well in this field was interpreted to verify the practicality of the proposed model.

https://doi.org/10.1021/acsomega.3c10360
ACS Omega 2024, 9, 17307−17322

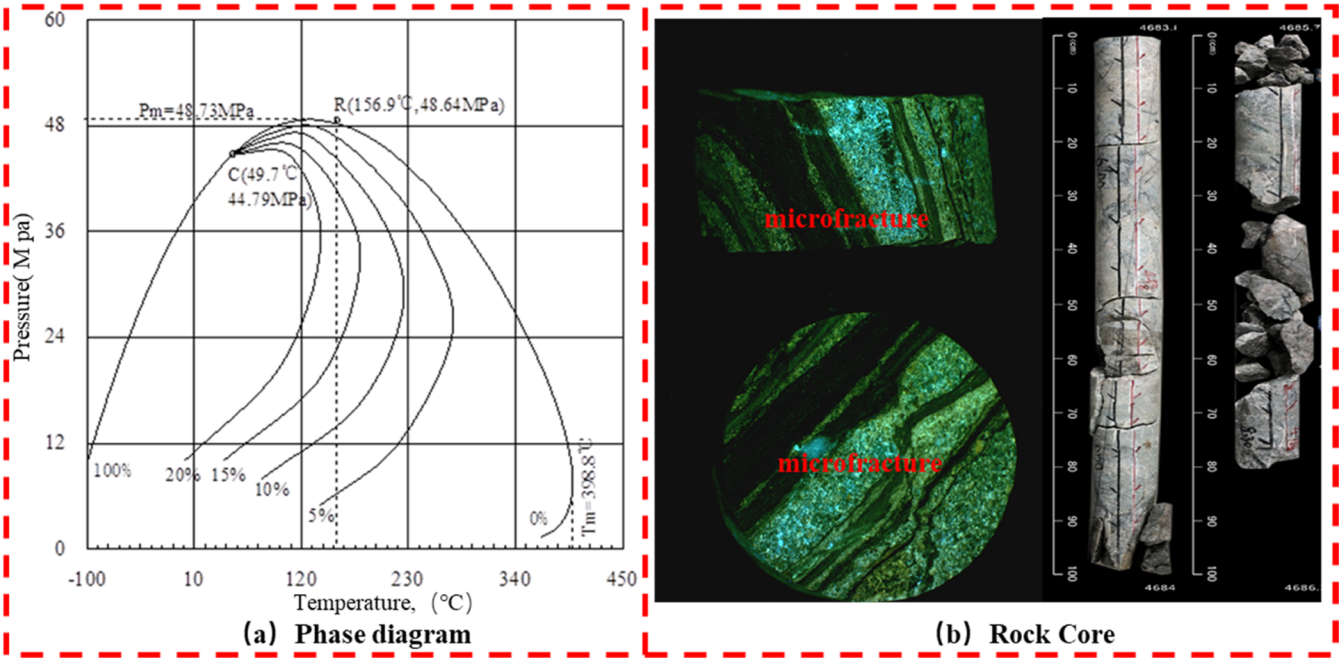

Figure 12. (a) Phase diagram and (b) the fracture characteristics observed in rock core.

Y gas condensate reservoir is a recently discovered large-capacity gas condensate reservoir in China. As shown in Figure 12a, the reservoir exhibits a maximum liquid pressure of 24.6% at a pressure of 26 MPa and a dew point pressure of 48.73 MPa. Formation coring has revealed the presence of natural fractures within the reservoir, as depicted in Figure 12b. Well X, a horizontal well within the gas condensate reservoir, exhibits a highly complex pressure measurement curve after a period of production with the fitting accuracy of existing models being inadequate. Consequently, the model proposed in this paper was employed for fitting analysis, yielding numerous parameters that could not be obtained via conventional models with a good fitting accuracy observed. Thus, the model presented in this paper demonstrates practicality for application in practice.

Table 2 presents the essential parameters of the gas condensate reservoir and well X, with the test conducted 3 years after the well was put into operation. Initially, the well produced solely natural gas. However, after 1 year of production, oil and gas were produced simultaneously. The semianalytical model proposed in this paper was employed to interpret the recorded pressure measurements, with Figure 13 illustrating a good fit between the recorded pressure measurements and the theoretical curve. The pressure curves recorded exhibit

Table 2. Basic Parameters of FGCR and Well X

parameters	value	sources
temperature, K	436.03	well logging
well depth, m	5126	well logging
original pressure, MPa	51.53	measurement
horizontal well length, m	300	
porosity, %	15.43	experiment
horizontal permeability, 10^{-3} μm^2	5.5	experiment measurement
vertical permeability, 10^{-3} μm^2	0.6	
reservoir thickness, m	80	
dew point pressure, MPa	42.1	experiment
maximum CVD liquid dropout,%	15	experiment measurement

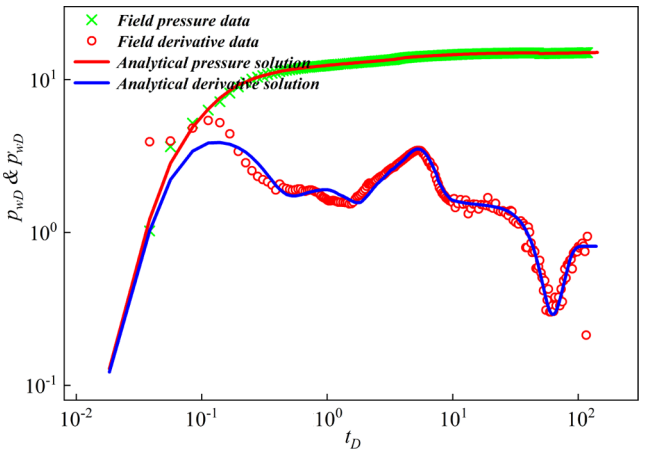

Figure 13. Application of the proposed semianalytical solution.

characteristics of flow between fractures and matrix, the production features of horizontal wells, and the intricacies of multizone complexities. The interpretation results are detailed in Table 3, with the model providing a comprehensive understanding of various parameters, including the physical properties of the formation and the radius of each retrograde condensate zone. As such, it aids in providing a more precise depiction of the condensate oil distribution within the reservoir and offers guidance for the development of gas condensate reservoirs.

6. CONCLUSIONS

A semianalytical model was developed in this study to examine the pressure behavior of horizontal wells in FGCR. A comprehensive account of the model development, validation, sensitivity analysis, and a case study was presented in detail. The semianalytical model is capable of interpreting pressure measurement data, assessing the current condensate distribution within the formation, and characterizing parameters such as fractures and effective production zones in horizontal wells. The

https://doi.org/10.1021/acsomega.3c10360
ACS Omega 2024, 9, 17307−17322

Table 3. Interpretations Results of Well X

parameters		symbol	unit	interpretation results
wellbore storage coefficient		C	m^3/MPa	0.58
skin factor		S		1.4
horizontal permeability	Zone I	k_1	10^{-3} μm^2	3.07
	Zone II	k_2		1.52
	Zone III	k_3		4.52
	Zone IV	k_4		5.31
composite radius	Zone I	R_1	m	201.63
	Zone II	R_2		361.26
	Zone III	R_3		426.21
Shape factor		λ		1×10^{-6}
Interporosity flow coefficient		ω		0.3
Permeability modulus		γ		0.001
Horizontal well length		L	m	300

utilization of this model is expected to considerably enhance the efficiency of FGCR development. Furthermore, a method is provided for accurately assessing the extent of retrograde condensation and determining the size of the retrograde condensate region utilizing the distinctive characteristics of the curve. In conclusion, this study makes valuable contributions to the field and highlights the importance of using the proposed model.

- We proposed a straightforward, swift, and robust semianalytical mathematical model tailored for a horizontal well dealing with multiphases (oil and gas), within the context of horizontal wells in FGCR. The derivation of our semianalytical approach is thoroughly discussed, and the numerical simulation results align admirably with outcomes from our model.
- Our model identifies 12 flow regimes, encompassing the wellbore storage phase, transitional flow stages, interporosity transitions, and various radial flow phases. The comparison between our numerical simulations and the proposed model showcases a commendable level of agreement overall.
- Notably, the wellbore storage coefficients significantly impact the early regime. Increasing the wellbore storage coefficients slows down the pressure drop, extends transitional flow periods, and delays the initiation and conclusion of the initial transition flow. Additionally, stress sensitivity manifests as an upturned curve characteristic in the later regime.
- The interporosity flow coefficient and composite radius can have an impact on the radial flow regime, potentially obscuring its distinctive characteristics. Specifically, the interporosity flow coefficient can alter the location of the interporosity regime, while the radial flow features of the latter zone may be masked when the radius of adjacent zones are similar.
- We conducted a case study in the Bozhong oil field, demonstrating that our model effectively interprets pressure measurements obtained from the FGCR. The proposed solution proves feasible for analyzing the radius of condensate oil and formation parameters.

APPENDIX A

Using the two-phase pseudopressure function introduced within the zone as an example, the differential equation for the seepage of condensate gas was linearized, and the subsequent two-phase pseudopressure integral function was introduced as follows:

$$\begin{cases} m_{1f}(p) = \int_{p_{wf}}^{p^*} \left(\frac{K_{rfo}}{\mu_o}\rho_o + \frac{K_{rfg}}{\mu_g}\rho_g \right) dp \\ m_{1m}(p) = \int_{p_{wf}}^{p^*} \left(\frac{K_{rmo}}{\mu_o}\rho_o + \frac{K_{rmg}}{\mu_g}\rho_g \right) dp \end{cases} \tag{A-1}$$

To simplify the differential equation for the unstable percolation of a condensate reservoir by introducing the two-phase pseudopressure function, the following equation transformation should be carried out initially:

$$\frac{\partial m_1(p)}{\partial r} = \frac{\partial m_1(p)}{\partial p}\cdot\frac{\partial p}{\partial r} = \left(\frac{K_{rfo}}{\mu_o}\rho_o + \frac{K_{rfg}}{\mu_g}\rho_g \right)\frac{\partial p}{\partial r} \tag{A-2}$$

Because of oil saturation, the density of oil and the density of gas are both functions of pressure:

$$\begin{aligned} \frac{\partial(S_{fo}\rho_o + S_{fg}\rho_g)}{\partial t} &= \frac{\partial(S_{fo}\rho_o + S_{fg}\rho_g)}{\partial p}\cdot\frac{\partial p}{\partial t} \\ &= \left[\left(\frac{\partial \rho_o}{\partial p}S_{fo} + \frac{\partial \rho_g}{\partial p}S_{fg} \right) + \left(\frac{\partial S_{fo}}{\partial p}\rho_o + \frac{\partial S_{fg}}{\partial p}\rho_g \right) \right]\cdot\frac{\partial p}{\partial t} \end{aligned} \tag{A-3}$$

The transform formulas $C_o = \frac{\partial \rho_o}{\partial p}\cdot\frac{1}{\rho_o}$, $C_g = \frac{\partial \rho_g}{\partial p}\cdot\frac{1}{\rho_g}$, and $S_{fo} + S_{fg} = 1$ can be used in eq A-3 to obtain

$$\frac{\partial(S_{fo}\rho_o + S_{fg}\rho_g)}{\partial t} = \left[(C_o\rho_o S_{fo} + C_g\rho_g S_{fg}) + (\rho_o - \rho_g)\frac{\partial S_{fo}}{\partial p} \right]\cdot\frac{\partial p}{\partial t} \tag{A-4}$$

In this work, we define C_{ft} as the total density compressibility, which is shown as $C_{ft} = C_o\rho_o S_{fo} + C_g\rho_o S_{fg}$, $C_{mt} = C_o\rho_o S_{mo} + C_g\rho_g S_{mg}$. Therefore,

$$\frac{\partial(S_{fo}\rho_o + S_{fg}\rho_g)}{\partial t} = \left[C_{ft} + (\rho_o - \rho_g)\frac{\partial S_{fo}}{\partial p} \right]\cdot\frac{\partial p}{\partial t} \tag{A-5}$$

$$\frac{\partial(S_{mo}\rho_o + S_{mg}\rho_g)}{\partial t} = \left[C_{mt} + (\rho_o - \rho_g)\frac{\partial S_{mo}}{\partial p} \right]\cdot\frac{\partial p}{\partial t} \tag{A-6}$$

Taking the derivative of pseudopressure function over time gives

$$\frac{\partial m_1(p)}{\partial t} = \frac{\partial m_1(p)}{\partial p}\cdot\frac{\partial p}{\partial t} = \left(\frac{K_{rfo}}{\mu_o}\rho_o + \frac{K_{rfg}}{\mu_g}\rho_g \right)\frac{\partial p}{\partial t} \tag{A-7}$$

Thus,

$$\frac{\partial p}{\partial t} = \frac{\partial m_{1f}(p)}{\partial t}\cdot\frac{1}{\left(\frac{K_{rfo}}{\mu_o}\rho_o + \frac{K_{rfg}}{\mu_g}\rho_g \right)} \tag{A-8}$$

$$\frac{\partial p}{\partial t} = \frac{\partial m_{1m}(p)}{\partial t}\cdot\frac{1}{\left(\frac{K_{rfo}}{\mu_o}\rho_o + \frac{K_{rfg}}{\mu_g}\rho_g \right)} \tag{A-9}$$

Substituting eqs A-1−A-9 into eq 1, we get

https://doi.org/10.1021/acsomega.3c10360
ACS Omega 2024, 9, 17307−17322

$$\begin{cases} \dfrac{K_{1fh}}{r}\dfrac{\partial}{\partial r}\left[re^{-\gamma(m_r-m)}\dfrac{\partial m_{1f}}{\partial r}\right] + K_{1fv}\dfrac{\partial}{\partial z}\left[re^{-\gamma(m_r-m)}\dfrac{\partial m_{1f}}{\partial z}\right] \\ \quad = \phi_f\dfrac{\left[C_{ft} + (\rho_o - \rho_g)\frac{\partial S_{fo}}{\partial p}\right]}{\left(\frac{K_{rfo}}{\mu_o}\rho_o + \frac{K_{rfg}}{\mu_g}\rho_g\right)}\dfrac{\partial m_{1f}}{\partial t} - F_s K_{1m}(m_{1m} - m_{1f}) \\ F_s K_{1m}(m_{1m} - m_{1f}) + \phi_m\dfrac{\left[C_{mt} + (\rho_o - \rho_g)\frac{\partial S_{mo}}{\partial p}\right]}{\left(\frac{K_{rfo}}{\mu_o}\rho_o + \frac{K_{rfg}}{\mu_g}\rho_g\right)}\cdot\dfrac{\partial m_{1m}}{\partial t} = 0 \end{cases} \tag{A-10}$$

The left-hand side of eq A-10 can be transformed as

$$\begin{aligned} &\frac{K_{1fh}}{r}\frac{\partial}{\partial r}\left[re^{-\gamma(m_r-m)}\frac{\partial m_{1f}}{\partial r}\right] = \frac{K_{1fh}}{r}\left[e^{-\gamma(m_r-m)}\frac{\partial m_{1f}}{\partial r}\right. \\ &\quad \left. + re^{-\gamma(m_r-m)}\gamma\left(\frac{\partial m_{1f}}{\partial r}\right)^2 + re^{-\gamma(m_r-m)}\frac{\partial m_{1f}^2}{\partial r^2}\right] \\ &\quad = e^{-\gamma(m_r-m)}\left[\frac{\partial m_{1f}^2}{\partial r^2} + \frac{1}{r}\frac{\partial m_{1f}}{\partial r} + \gamma\left(\frac{\partial m_{1f}}{\partial r}\right)^2\right] \end{aligned} \tag{A-11}$$

$$\begin{aligned} &K_{1fv}\frac{\partial}{\partial z}\left[re^{-\gamma(m_r-m)}\frac{\partial m_{1f}}{\partial z}\right] = K_{1fv}\left[e^{-\gamma(m_r-m)}\gamma\left(\frac{\partial m_{1f}}{\partial z}\right)^2\right. \\ &\quad \left. + e^{-\gamma(m_r-m)}\frac{\partial m_{1f}^2}{\partial z^2}\right] = K_{1fv}e^{-\gamma(m_r-m)}\left[\frac{\partial m_{1f}^2}{\partial z^2} + \gamma\left(\frac{\partial m_{1f}}{\partial z}\right)^2\right] \end{aligned} \tag{A-12}$$

Then the following equation can be obtained:

$$\begin{aligned} &\left[\frac{\partial m_{1f}^2}{\partial r^2} + \frac{1}{r}\frac{\partial m_{1f}}{\partial r} + \gamma\left(\frac{\partial m_{1f}}{\partial r}\right)^2\right] + \frac{K_{1fv}}{K_{1fh}}\left[\frac{\partial m_{1f}^2}{\partial z^2} + \gamma\left(\frac{\partial m_{1f}}{\partial z}\right)^2\right] \\ &\quad = e^{\gamma(m_r-m)}\left\{\frac{\partial m_{1m}}{\partial t}\frac{\phi_f}{K_{1fh}}\frac{\left[C_{tf} + (\rho_o - \rho_g)\frac{\partial S_{fo}}{\partial p}\right]}{\left(\frac{K_{rfo}}{\mu_o}\rho_o + \frac{K_{rfg}}{\mu_g}\rho_g\right)}\cdot\frac{\partial m_{1f}}{\partial t}\right. \\ &\quad \left. + \frac{\phi_m}{K_{1fh}}\frac{\left[C_{tm} + (\rho_o - \rho_g)\frac{\partial S_{mo}}{\partial p}\right]}{\left(\frac{K_{rfo}}{\mu_o}\rho_o + \frac{K_{rfg}}{\mu_g}\rho_g\right)}\cdot\frac{\partial m_{1m}}{\partial t}\right\} \end{aligned} \tag{A-13}$$

Finally, eq A-10 becomes

$$\begin{cases} \left[\dfrac{\partial m_{1f}^2}{\partial r^2} + \dfrac{1}{r}\dfrac{\partial m_{1f}}{\partial r} + \gamma\left(\dfrac{\partial m_{1f}}{\partial r}\right)^2\right] + \dfrac{K_{1fv}}{K_{1fh}}\left[\dfrac{\partial m_{1f}^2}{\partial z^2} + \gamma\left(\dfrac{\partial m_{1f}}{\partial z}\right)^2\right] \\ \quad = e^{\gamma(m_r-m)}\left\{\dfrac{1}{\xi_{1f}}\cdot\dfrac{\partial m_{1f}}{\partial t} + \dfrac{1}{\xi_{1m}}\cdot\dfrac{\partial m_{1m}}{\partial t}\right\} \\ F_s K_{1m}(m_{1m} - m_{1f}) + \dfrac{K_{1fh}}{\xi_{1m}}\cdot\dfrac{\partial m_{1m}}{\partial t} = 0 \end{cases} \tag{A-14}$$

where

$$\begin{aligned} \xi_{1f} &= \frac{K_{1fh}}{\phi_f}\cdot\frac{\left(\frac{K_{rfo}}{\mu_o}\rho_o + \frac{K_{rfg}}{\mu_g}\rho_g\right)}{\left[C_{tf} + (\rho_o - \rho_g)\frac{\partial S_{fo}}{\partial p}\right]} \\ \xi_{1m} &= \frac{K_{1fh}}{\phi_m}\cdot\frac{\left(\frac{K_{rfo}}{\mu_o}\rho_o + \frac{K_{rfg}}{\mu_g}\rho_g\right)}{\left[C_{tm} + (\rho_o - \rho_g)\frac{\partial S_{mo}}{\partial p}\right]} \end{aligned} \tag{A-15}$$

APPENDIX B

We define the following dimensionless variables:

$$m_{ifD} = \frac{K_{ifh}h[m_{if}(p_0) - m_{if}(p_j)]}{q_t} \quad (i = 1, 2, 3, 4)$$

$$m_{imD} = \frac{K_{imh}h[m_{im}(p_0) - m_{im}(p_j)]}{q_t} \quad (i = 1, 2, 3, 4)$$

$$\lambda = F_s\frac{K_{1m}}{K_{1fh}}r_w^2 \qquad \omega = \frac{\phi_f C_{ft}}{\phi_f C_{ft} + \phi_m C_{mt}} \qquad \gamma_D = \frac{q_t}{K_{1fh}h}\gamma$$

$$t_D = \frac{\xi_{1f}t}{(\xi_{1f} + \xi_{1m})L^2} \qquad C_D = \frac{C}{(\phi_f C_{1ft} + \phi_m C_{1mt})hL^2}$$

$$L_D = \frac{L}{h}\sqrt{\frac{K_{1fh}}{K_{1fv}}} \qquad h_D = \frac{h}{r_w}\sqrt{\frac{K_{1fh}}{K_{1fv}}}$$

$$r_D = \frac{r}{L} \qquad r_{wD} = \frac{r_w}{L} \qquad z_D = \frac{z}{h} \qquad z_{wD} = \frac{z_w}{h}$$

$$M_1 = 1 \qquad M_2 = \frac{\xi_{1f}}{\xi_{2f}} \qquad M_3 = \frac{\xi_{1f}}{\xi_{3f}} \qquad M_4 = \frac{\xi_{1f}}{\xi_{4f}}$$

$$q_t = q_o\rho_o + q_g\rho_g$$

APPENDIX C

The diffusivity equation is not presented in a form that is amenable to analytical solution. To address this issue, a new dimensionless dependent variable is introduced, which is linked to the dimensionless pressure:[40]

$$m_{fD}(r_D, z_D, t_D) = -\frac{1}{\gamma_D}\ln[1 - \gamma_D\eta_D(r_D, z_D, t_D)] \tag{C-1}$$

By utilizing the Pedrosa variable substitution (eq C-2), the subsequent partial differential equation can be derived (i = 1, 2, 3, 4):

$$\begin{aligned} &\frac{1}{r_D}\frac{\partial}{\partial r_D}\left(r_D\frac{\partial \eta_{ifD}}{\partial r_D}\right) + L_D^2\frac{\partial^2\eta_{ifD}}{\partial z_D^2} = (h_D L_D)^2\left[(1 - \omega)\frac{\partial m_{imD}}{\partial t_D}\right. \\ &\quad \left. + M_i\frac{\omega}{1 - \gamma_D\eta_{ifD}}\frac{\partial m_{ifD}}{\partial t_D}\right] \end{aligned}$$

$$(1 - \omega)\frac{\partial m_{imD}}{\partial t_D} + \lambda[m_{imD} + \ln(1 - \gamma_D\eta_{ifD})] = 0$$

$$\eta_{1fD}(r_{D1}, t_D) = \eta_{2fD}(r_{D1}, t_D)$$

https://doi.org/10.1021/acsomega.3c10360
ACS Omega 2024, 9, 17307−17322

$$\left.\frac{\partial \eta_{1fD}}{\partial r_D}\right|_{r_D=r_{D1}} = \left.\frac{1}{M_2}\frac{\partial \eta_{2fD}}{\partial r_D}\right|_{r_D=r_{D1}}$$

$$\eta_{2fD}(r_{D2}, t_D) = \eta_{3fD}(r_{D2}, t_D)$$

$$\left.\frac{\partial \eta_{2fD}}{\partial r_D}\right|_{r_D=r_{D2}} = \left.\frac{M_2}{M_3}\frac{\partial \eta_{3fD}}{\partial r_D}\right|_{r_D=r_{D2}}$$

$$\eta_{3fD}(r_{D3}, t_D) = \eta_{4fD}(r_{D3}, t_D)$$

$$\left.\frac{\partial \eta_{3fD}}{\partial r_D}\right|_{r_D=r_{D3}} = \left.\frac{M_3}{M_4}\frac{\partial \eta_{4fD}}{\partial r_D}\right|_{r_D=r_{D3}}$$

$$\eta_{ifD}(r_D, 0) = \eta_{imD}(r_D, 0) = 0,$$

$$\eta_{4fD}(\infty, t_D) = \eta_{4mD}(\infty, t_D) = 0$$

$$\lim_{\varepsilon_D\to 0}\left[\lim_{r_D\to 0}\int_{z_{wD}-\varepsilon_D/2}^{z_{wD}+\varepsilon_D/2}\left(r_D e^{-\gamma_D\eta_{ifD}}\frac{\partial \eta_{1fD}}{\partial r_D}\right)dz_{wD}\right] = \frac{1}{2},$$
$$|z_D - z_{wD}| \le \frac{\varepsilon_D}{2}$$

$$\left.\frac{\partial \eta_{1fD}}{\partial z_D}\right|_{z_D=r_{D1}} = \left.\frac{\partial \eta_{1mD}}{\partial z_D}\right|_{z_D=0} = 0$$

$$\left.\frac{\partial \eta_{1fD}}{\partial z_D}\right|_{z_D=r_{D1}} = \left.\frac{\partial \eta_{1mD}}{\partial z_D}\right|_{z_D=1} = 0 \quad \text{(C-2)}$$

To obtain an approximate analytical solution, the perturbation law is employed. As the dimensionless permeability modulus is typically small, η can be expanded as a power series in the parameter γ_D:[41,42]

$$\begin{cases}\eta_D = \eta_0 + \gamma_D\eta_1 + \gamma_D^2\eta_2 + \cdots \\ \dfrac{1}{1-\gamma_D\eta} = 1 + \gamma_D\eta + \gamma_D^2\eta_2^2 + \cdots\end{cases} \quad \text{(C-3)}$$

Upon substitution of eq C-3 into eqs C-2, eqs C-2 can be represented in the Laplace space as follows (i = 1, 2, 3, 4):

$$\frac{1}{r_D}\frac{\partial}{\partial r_D}\left(r_D\frac{\partial \eta_{ifD}}{\partial r_D}\right) + L_D^2\frac{\partial^2\eta_{ifD}}{\partial z_D^2} = (h_D L_D)^2\left[(1-\omega)\frac{\partial m_{imD}}{\partial t_D} + M_{i\omega}\frac{\partial m_{ifD}}{\partial t_D}\right]$$

$$(1-\omega)\frac{\partial m_{imD}}{\partial t_D} + \lambda(m_{imD} + \eta_{ifD}) = 0$$

$$\eta_{1fD}(r_{D1}, t_D) = \eta_{2fD}(r_{D1}, t_D)$$

$$\left.\frac{\partial \eta_{1fD}}{\partial r_D}\right|_{r_D=r_{D1}} = \left.\frac{1}{M_2}\frac{\partial \eta_{2fD}}{\partial r_D}\right|_{r_D=r_{D1}}$$

$$\eta_{2fD}(r_{D2}, t_D) = \eta_{3fD}(r_{D2}, t_D)$$

$$\left.\frac{\partial \eta_{2fD}}{\partial r_D}\right|_{r_D=r_{D2}} = \left.\frac{M_2}{M_3}\frac{\partial \eta_{3fD}}{\partial r_D}\right|_{r_D=r_{D2}}$$

$$\eta_{3fD}(r_{D3}, t_D) = \eta_{4fD}(r_{D3}, t_D)$$

$$\left.\frac{\partial \eta_{3fD}}{\partial r_D}\right|_{r_D=r_{D3}} = \left.\frac{M_3}{M_4}\frac{\partial \eta_{4fD}}{\partial r_D}\right|_{r_D=r_{D3}}$$

$$\eta_{ifD}(r_D, 0) = \eta_{imD}(r_D, 0) = 0,$$

$$\eta_{4fD}(\infty, t_D) = \eta_{4mD}(\infty, t_D) = 0$$

$$\lim_{\varepsilon_D\to 0}\left[\lim_{r_D\to 0}\int_{z_{wD}-\varepsilon_D}^{z_{wD}+\varepsilon_D}\left(r_D e^{-\gamma_D\eta_{ifD}}\frac{\partial \eta_{1fD}}{\partial r_D}\right)dz_{wD}\right] = \frac{1}{2},$$
$$|z_D - z_{wD}| \le \frac{\varepsilon_D}{2}$$

$$\left.\frac{\partial \eta_{1fD}}{\partial z_D}\right|_{z_D=r_{D1}} = \left.\frac{\partial \eta_{1mD}}{\partial z_D}\right|_{z_D=0} = 0$$

$$\left.\frac{\partial \eta_{1fD}}{\partial z_D}\right|_{z_D=r_{D1}} = \left.\frac{\partial \eta_{1mD}}{\partial z_D}\right|_{z_D=1} = 0 \quad \text{(C-4)}$$

In order to achieve analytical solution, the Laplace transformation needs to be performed to transform the model into ordinary differential equations. After application of the Laplace transformation with respect to t_D, the dimensionless model in the Laplace domain can be expressed as

$$\frac{1}{r_D}\frac{\partial}{\partial r_D}\left(r_D\frac{\partial \eta_{ifD}}{\partial r_D}\right) + L_D^2\frac{\partial^2\eta_{ifD}}{\partial z_D^2} = (h_D L_D)^2[(1-\omega)u\partial\overline{m}_{imD} + M_i\omega u\partial\overline{\eta}_{ifD}]$$

$$M_i(1-\omega)u\overline{m}_{imD} + \lambda(\overline{m}_{imD} + \overline{\eta}_{ifD}) = 0$$

$$\overline{\eta}_{1fD}(r_{D1}, t_D) = \overline{\eta}_{2fD}(r_{D1}, t_D)$$

$$\left.\frac{\partial \overline{\eta}_{1fD}}{\partial r_D}\right|_{r_D=r_{D1}} = \left.\frac{1}{M_2}\frac{\partial \overline{\eta}_{2fD}}{\partial r_D}\right|_{r_D=r_{D1}}$$

$$\overline{\eta}_{2fD}(r_{D2}, t_D) = \overline{\eta}_{3fD}(r_{D2}, t_D)$$

$$\left.\frac{\partial \overline{\eta}_{2fD}}{\partial r_D}\right|_{r_D=r_{D2}} = \left.\frac{M_2}{M_3}\frac{\partial \overline{\eta}_{3fD}}{\partial r_D}\right|_{r_D=r_{D2}}$$

$$\overline{\eta}_{3fD}(r_{D3}, t_D) = \overline{\eta}_{4fD}(r_{D3}, t_D)$$

$$\left.\frac{\partial \overline{\eta}_{3fD}}{\partial r_D}\right|_{r_D=r_{D3}} = \left.\frac{M_3}{M_4}\frac{\partial \overline{\eta}_{4fD}}{\partial r_D}\right|_{r_D=r_{D3}}$$

$$\overline{\eta}_{ifD}(r_D, 0) = \overline{m}_{imD}(r_D, 0) = 0$$

$$\overline{\eta}_{4fD}(\infty, t_D) = \overline{m}_{4mD}(\infty, t_D) = 0$$

https://doi.org/10.1021/acsomega.3c10360
ACS Omega 2024, 9, 17307−17322

$$\lim_{\varepsilon_D\to 0}\left[\lim_{r_D\to 0}\int_{z_{wD}-\varepsilon_D/2}^{z_{wD}+\varepsilon_D/2}\left(r_D\frac{\partial\overline{\eta}_{1fD}}{\partial r_D}\right)dz_{wD}\right]=\frac{1}{2},\quad |z_D-z_{wD}|\le\frac{\varepsilon_D}{2}$$

$$\left.\frac{\partial\overline{\eta}_{1fD}}{\partial z_D}\right|_{z_D=r_{D1}}=\left.\frac{\overline{m}_{1mD}}{\partial z_D}\right|_{z_D=0}=0$$

$$\left.\frac{\partial\overline{\eta}_{1fD}}{\partial z_D}\right|_{z_D=r_{D1}}=\left.\frac{\overline{m}_{1mD}}{\partial z_D}\right|_{z_D=1}=0 \tag{C-5}$$

To obtain the point source solution, eq C-6 can be utilized by performing a finite cosine transform with respect to z_D:[43]

$$G[\overline{\eta}_{ifD}(r_D,z_D,u)]=\overline{\eta}_{ifD}(r_D,n,u)=\int_0^1\overline{\eta}_{ifD}(r_D,z_D,u)\cos(n\pi z_D)dz_D \tag{C-6}$$

The inverse finite cosine transform with respect to z_D is expressed as

$$G^{-1}[\overline{\eta}_{ifD}(r_D,n,u)]=\overline{\eta}_{ifD}(r_D,z_D,u)=\int_0^1\frac{\cos(n\pi z_D)}{N(n)}\overline{\eta}_{ifD}(r_D,n,u)dz_D \tag{C-7}$$

where

$$N(n)=\int_0^1\cos^2(n\pi z_D)dz_D=\begin{cases}1, & n=0\\ 1/2, & n\neq 0\end{cases} \tag{C-8}$$

Performing the finite cosine transform of eq C-5 (i = 1, 2, 3, 4) yields

$$\begin{cases}\frac{1}{r_D}\frac{d}{dr_D}\left(r_D\frac{d\overline{\eta}_{ifD}}{dr_D}\right)=[uf_i(u)(h_DL_D)^2+(n\pi L_D)^2]\overline{\eta}_{ifD}\\ \lim\limits_{r_D\to 0}r_D\frac{d\overline{\eta}_{ifD}}{dr_D}=\frac{-\cos(n\pi z_{wD})}{2u}\end{cases} \tag{C-9}$$

where

$$f_i(u)=\frac{M_i[\lambda+\omega(1-\omega)u]}{M_i\omega(1-\omega)+\lambda} \tag{C-10}$$

The solution to eq C-9 (i = 1, 2, 3, 4) in the Laplace domain, employing Bessel functions, is expressed as[44]

$$\overline{\eta}_{ifD}=A_iK_0(r_D\cdot\sqrt{F_i(u)})+B_iI_0(r_D\cdot\sqrt{F_i(u)}) \tag{C-11}$$

where

$$F_{in}(u)=uf_i(u)(h_DL_D)^2+(n\pi L_D)^2 \tag{C-12}$$

According to the outer boundary condition and the inner boundary condition, we know that

$$\overline{\eta}_{4fD}(\infty,t_D)=A_4K_0(r_D\cdot\sqrt{F_4(u)})+B_4I_0(r_D\cdot\sqrt{F_4(u)})=0 \tag{C-13}$$

$$\lim_{r_D\to 0}r_D\frac{d\overline{\eta}_{ifD}}{dr_D}=\lim_{r_D\to 0}r_D[-A_1K_1\sqrt{F_1(u)}(r_D\cdot\sqrt{F_1(u)})+B_1I_1\sqrt{F_1(u)}(r_D\cdot\sqrt{F_1(u)})]=\frac{-\cos(n\pi z_{wD})}{2u} \tag{C-14}$$

Because of the property of Bessel functions,

$$A_1=\frac{-\cos(n\pi z_{wD})}{2u},\quad B_4=0 \tag{C-15}$$

According to the interface conditions between different regions, we can get:

$$\begin{aligned}
&A_1K_0(r_{D1}\cdot\sqrt{F_1(u)})+B_1I_0(r_{D1}\cdot\sqrt{F_1(u)})=A_2K_0(r_{D1}\cdot\sqrt{F_2(u)})+B_2I_0(r_{D1}\cdot\sqrt{F_2(u)})\\
&A_2K_0(r_{D2}\cdot\sqrt{F_2(u)})+B_2I_0(r_{D2}\cdot\sqrt{F_2(u)})=A_3K_0(r_{D2}\cdot\sqrt{F_3(u)})+B_3I_0(r_{D2}\cdot\sqrt{F_3(u)})\\
&A_3K_0(r_{D3}\cdot\sqrt{F_3(u)})+B_3I_0(r_{D3}\cdot\sqrt{F_3(u)})=A_4K_0(r_{D3}\cdot\sqrt{F_4(u)})\\
&-A_1\sqrt{F_1(u)}K_1(r_{D1}\cdot\sqrt{F_1(u)})+B_1\sqrt{F_1(u)}I_1(r_{D1}\cdot\sqrt{F_1(u)})=\frac{1}{M_2}[-A_2\sqrt{F_2(u)}K_1(r_{D1}\cdot\sqrt{F_2(u)})+B_2\sqrt{F_2(u)}I_1(r_{D1}\cdot\sqrt{F_2(u)})]\\
&-A_2\sqrt{F_2(u)}K_1(r_{D2}\cdot\sqrt{F_1(u)})+B_2\sqrt{F_2(u)}I_1(r_{D2}\cdot\sqrt{F_2(u)})=\frac{M_2}{M_3}[-A_3\sqrt{F_3(u)}K_1(r_{D2}\cdot\sqrt{F_3(u)})+B_3\sqrt{F_3(u)}I_1(r_{D2}\cdot\sqrt{F_3(u)})]\\
&-A_3\sqrt{F_3(u)}K_1(r_{D3}\cdot\sqrt{F_3(u)})+B_3\sqrt{F_3(u)}I_1(r_{D3}\cdot\sqrt{F_3(u)})=\frac{M_3}{M_4}[-A_4\sqrt{F_4(u)}K_1(r_{D3}\cdot\sqrt{F_4(u)})]
\end{aligned} \tag{C-16}$$

Equation C-16 contains six equations and six unknown variables (A_2, A_3, A_4, B_1, B_2, B_3) and thus is a solvable equation set. We define the following variables for the convenience of solving the equation set:

$$\begin{aligned}
&a_{11}=K_0(r_{D1}\cdot\sqrt{F_1(u)}),\quad a_{12}=I_0(r_{D1}\cdot\sqrt{F_1(u)})\\
&a_{13}=K_0(r_{D1}\cdot\sqrt{F_2(u)}),\quad a_{14}=I_0(r_{D1}\cdot\sqrt{F_2(u)})\\
&a_{23}=K_0(r_{D2}\cdot\sqrt{F_2(u)}),\quad a_{24}=I_0(r_{D2}\cdot\sqrt{F_2(u)})\\
&a_{25}=K_0(r_{D1}\cdot\sqrt{F_2(u)}),\quad a_{26}=I_0(r_{D2}\cdot\sqrt{F_3(u)})\\
&a_{35}=K_0(r_{D3}\cdot\sqrt{F_3(u)}),\quad a_{36}=I_0(r_{D3}\cdot\sqrt{F_3(u)})\\
&a_{37}=K_0(r_{D3}\cdot\sqrt{F_4(u)})\\
&a_{41}=-\sqrt{F_1(u)}K_1(r_{D1}\cdot\sqrt{F_1(u)})\\
&a_{42}=\sqrt{F_1(u)}I_1(r_{D1}\cdot\sqrt{F_1(u)})\\
&a_{43}=-\frac{1}{M_2}\sqrt{F_2(u)}K_1(r_{D1}\cdot\sqrt{F_2(u)})
\end{aligned}$$

https://doi.org/10.1021/acsomega.3c10360
ACS Omega 2024, 9, 17307−17322

$$a_{44} = \frac{1}{M_2}\sqrt{F_2(u)}\, I_1(r_{D1}\cdot\sqrt{F_2(u)})$$

$$a_{53} = -\sqrt{F_2(u)}\, K_1(r_{D2}\cdot\sqrt{F_1(u)})$$

$$a_{54} = \sqrt{F_2(u)}\, I_1(r_{D2}\cdot\sqrt{F_2(u)})$$

$$a_{55} = -\frac{M_2}{M_3}\sqrt{F_3(u)}\, K_1(r_{D2}\cdot\sqrt{F_3(u)})$$

$$a_{56} = \frac{M_2}{M_3}\sqrt{F_3(u)}\, I_1(r_{D2}\cdot\sqrt{F_3(u)})$$

$$a_{65} = -\sqrt{F_3(u)}\, K_1(r_{D3}\cdot\sqrt{F_3(u)})$$

$$a_{66} = \sqrt{F_3(u)}\, I_1(r_{D3}\cdot\sqrt{F_3(u)})$$

$$a_{67} = -\frac{M_3}{M_4}[\sqrt{F_4(u)}\, K_1(r_{D3}\cdot\sqrt{F_4(u)})] \tag{C-17}$$

By solving the above simplified equation set, we can obtain

$$B_1 = gA_1 = g\frac{\cos(n\pi z_{wD})}{2u} \tag{C-18}$$

where

$$g = \frac{ba_{14}}{aa_{14}}$$

$$ba_{14} = \frac{(a_{43}\cdot aa_{24} + a_{44}\cdot ba_{24}) - \frac{a_{41}}{a_{11}}(a_{13}\cdot aa_{24} + a_{14}\cdot ba_{24})}{a_{42} - a_{12}\frac{a_{41}}{a_{11}}}$$

$$aa_{14} = \frac{(a_{43}\cdot aa_{24} + a_{44}\cdot ba_{24}) - \frac{a_{42}}{a_{12}}(a_{13}\cdot aa_{24} + a_{14}\cdot ba_{24})}{a_{41} - a_{11}\frac{a_{42}}{a_{12}}}$$

$$ba_{24} = \frac{(a_{55}\cdot aa_{34} + a_{56}\cdot ba_{34}) - \frac{a_{53}}{a_{23}}(a_{25}\cdot aa_{34} + a_{26}\cdot ba_{34})}{a_{54} - a_{24}\frac{a_{53}}{a_{23}}}$$

$$aa_{24} = \frac{(a_{55}\cdot aa_{34} + a_{56}\cdot ba_{34}) - \frac{a_{54}}{a_{24}}(a_{25}\cdot aa_{34} + a_{26}\cdot ba_{34})}{a_{53} - a_{23}\frac{a_{54}}{a_{24}}}$$

$$aa_{34} = \frac{(a_{37} - a_{67}\cdot a_{36}/a_{66})}{a_{35} - a_{65}\frac{a_{36}}{a_{66}}}$$

$$ba_{34} = \frac{(a_{37} - a_{67}\cdot a_{35}/a_{65})}{a_{36} - a_{66}\frac{a_{35}}{a_{65}}} \tag{C-19}$$

Consequently, we have solved A_1 and B_1, so the solution in region-1 can be expressed as

$$\begin{aligned}\overline{\eta}_{ifD} &= A_1K_0(r_D\cdot\sqrt{F_1(u)}) + B_1I_0(r_D\cdot\sqrt{F_1(u)}) \\ &= \frac{\cos(n\pi z_{wD})}{2u}[K_0(r_D\sqrt{f_1^n(u)}) + gI_0(r_D\sqrt{f_1^n(u)})]\end{aligned} \tag{C-20}$$

In order to obtain the point source solution, we applied the cosine transformation to simplify the original model, so we need to apply the inverse cosine transformation after gaining the point source solution:[40]

$$\begin{aligned}\overline{\eta}_{wDN} = &\int_{-1}^{1}\frac{1}{2u}[K_0(r_D\sqrt{F_1^0(u)}) + gI_0(r_D\sqrt{F_1^0(u)})]dz_{wD} \\ &+ \int_{-1}^{1}\sum_{1}^{\infty}\frac{\cos(n\pi z_D)\cos(n\pi z_{wD})}{u}[K_0(r_D\sqrt{F_1^n(u)}) \\ &+ gI_0(r_D\sqrt{F_1^n(u)})]dz_{wD}\end{aligned} \tag{C-21}$$

where $r_D = \sqrt{(x_D - x_{wD})^2 + (y_D - y_{wD})^2}$.

AUTHOR INFORMATION

Corresponding Author

Fuguo Yin − *State Key Laboratory of Petroleum Resources and Engineering, China University of Petroleum Beijing, Beijing 102249, China;* orcid.org/0009-0005-4646-741X; Email: cupb65265764@163.com

Authors

Shiqing Cheng − *State Key Laboratory of Petroleum Resources and Engineering, China University of Petroleum Beijing, Beijing 102249, China;* orcid.org/0000-0001-5267-5569

Wenpeng Bai − *State Key Laboratory of Petroleum Resources and Engineering, China University of Petroleum Beijing, Beijing 102249, China*

Yang Wang − *State Key Laboratory of Petroleum Resources and Engineering, China University of Petroleum Beijing, Beijing 102249, China;* orcid.org/0000-0002-0349-2632

Xiuwei Liu − *State Key Laboratory of Petroleum Resources and Engineering, China University of Petroleum Beijing, Beijing 102249, China*

Complete contact information is available at: https://pubs.acs.org/10.1021/acsomega.3c10360

Notes

The authors declare no competing financial interest.

ACKNOWLEDGMENTS

The authors thank the editors and reviewers for their valuable suggestions and important contributions to the improvement of this manuscript. They acknowledge the financial support from the Strategic Cooperation Technology Projects of CNOOC and CUPB (CCL2021RCPS0298RSN).

NOMENCLATURE

γ = permeability modulus, mPa·s/MPa^2
γ_D = dimensionless permeability modulus
K_{ifh} = zone i horizontal permeability in the fractures, 10^{-3} μm^2
K_{ifv} = zone i vertical permeability in the fractures, 10^{-3} μm^2
K_{im} = zone i permeability in the matrix, 10^{-3} μm^2
K_{rfg} = relative permeability of gas in the fractures, 10^{-3} μm^2
K_{rmg} = relative permeability of gas in the matrix, 10^{-3} μm^2
K_{rfo} = relative permeability of oil in the fractures, 10^{-3} μm^2
K_{rmo} = relative permeability of oil in the matrix, 10^{-3} μm^2
ϕ_m = matrix system porosity, %
ϕ_f = fracture system porosity, %
μ_g = gas viscosity, mPa·s
μ_o = oil viscosity, mPa·s
S_{fo} = oil saturation in the fractures, %
S_{fg} = gas saturation in the fractures, %
S_{mo} = oil saturation in the matrix, %

https://doi.org/10.1021/acsomega.3c10360
ACS Omega 2024, 9, 17307−17322

S_{mg} = gas saturation in the matrix, %
C_{ft} = total compressibility in the fractures, MPa^{-1}
C_{mt} = total compressibility in the matrix, MPa^{-1}
C_o = oil compressibility, MPa^{-1}
C_g = gas compressibility, MPa^{-1}
ρ_o = oil density
ρ_g = gas density
p_m = pressure in the matrix, MPa
p_{Dm} = dimensionless matrix pressure
p_f = pressure in the fracture, MPa
p_{Df} = dimensionless fracture pressure
p_r = initial reservoir pressure, MPa
m = pseudopressure function, $kg/(m^3 \cdot s)$,
Ψ = dimensionless pseudopressure function
C = wellbore storage coefficient, m^3/MPa
C_D = dimensionless wellbore storage coefficient
F_s = shape factor
t = time, h
t_D = dimensionless time
r_w = wellbore radius, m
r = radial distance, m
r_D = dimensionless radial distance
z = vertical distance, m
z_D = dimensionless vertical distance
h = reservoir thickness, m
L = half-length of horizontal well, m
q_t = total mass production rate, kg/s
S = skin factor
λ = interporosity flow coefficient interporosity flow coefficient
ω = storativity
M_{if} = zone i mobility
η_{if} = zone i storability, m^2/s
η_{if} = zone i storability, m^2/s
ζ = Pedrosa variable
A, B = coefficients of Bessel function

SPECIAL FUNCTIONS

$I_0(x)$ =Bessel function of the first kind
$K_0(x)$ =Bessel function of the second kind
$F(x)$ =finite cosine transform
$F^{-1}(x)$ =inverse finite cosine transform

SUBSCRIPTS

i =zone i
D =dimensionless
f =fracture system
m =matrix system
u =Laplace variable
—— =Laplace space
$\wedge$ =finite cosine variable

REFERENCES

(1) Guo, P.; Li, S. L. Status and issues of techcologies for development of gas condensate pools(in Chinese). *Xinjiang Pet. Geol.* **2002**, *23* (3), 262−264.
(2) Yang, D. B.; Zhu, G. Y.; Liu, J. J. Distribution of global condensate gas field and major factors controlling its for-mation(in Chinese). *Earth Sci. Front.* **2010**, *17* (1), 339−349.
(3) Roussennac, B. Gas Condensate Well Test Analysis. M.S. Thesis, Stanford University, 2001.
(4) Kamari, A.; Li, L.; Sheng, J. J. Effects of rock pore sizes on the PVT properties of oil and gas-condensates in shale and tight reservoirs. *Petroleum* **2018**, *4* (2), 148−157.
(5) Zou, C. N.; Tao, S. Z. The geological characteristics of gas reservoir in China(in Chinese). *Sci. China Press* **2007**, *037* (0z2), 12−28.
(6) Novosad, Z. Composition and phase changes in testing and producing retrograde gas wells. *SPE Reservoir Eng.* **1996**, *11* (04), 231−235.
(7) Gringarten, A. C.; Ramey, H. J. The Use of Source and Green's Functions in Solving Unsteady-Flow Problems in Reservoirs. *Soc. Pet. Eng. J.* **1973**, *13*, 285−296, DOI: 10.2118/3818-PA.
(8) Daviau, F.; Mouronval, G.; Bourdarot, G.; Curutchet, P. Pressure Analysis for Horizontal Wells. *SPE Form. Eval.* **1988**, *3*, 716−724.
(9) Goode, P. A.; Thambynayagam, R. K. M. Pressure Drawdown and Buildup Analysis of Horizontal Wells in Anisotropic Media. *SPE Form. Eval.* **1987**, *2*, 683−697.
(10) Dougherty, E. L.; Lombardino, E.; Goode, P. A.; Zagalai, B. A Method for Simulating Pressure/Production Performance of Volumetric Dry Gas Reservoirs. *J. Pet. Technol.* **1985**, *37*, 2059−2070.
(11) Ozkan, E.; Raghavan, R.; Joshi, S. D. *Horizontal Well Pressure Analysis*, Paper presented at the SPE California Regional Meeting; OnePetro: Ventura, CA, 1987.
(12) Ozkan, E.; Raghavan, R.; Joshl, S. D. Horizontal-Well Pressure Analysis. *SPE Form. Eval.* **1989**, *4*, 567−575.
(13) Ozkan, E.; Raghavan, R. Performance of Horizontal Wells Subject to Bottomwater Drive. *SPE Res. Eng.* **1990**, *5*, 375−383, DOI: 10.2118/18559-PA.
(14) Ozkan, E.; Raghavan, R. New Solutions for Well-Test-Analysis Problems: Part 1—Analytical Considerations. *SPE Form. Eval.* **1991**, *6*, 359−368.
(15) Ozkan, E.L.; Raghavan, R. New Solutions for Well-Test-Analysis Problems: Part 2 — Computational Considerations and Applications. *SPE Form. Eval.* **1991**, *6*, 369−378.
(16) Ozkan, E.; Raghavan, R. *New Solutions for Well-Test-Analysis Problems: Part III—Additional Algorithms*, SPE Annual Technical Conference and Exhibition; OnePetro: New Orleans, LA, 1994.
(17) Marir, B.; Tiab, D. *Performance of Horizontal Wells in Gas Condensate Reservoirs: Hassi R'Mel Field, Algeria*, SPE Russian Oil and Gas Technical Conference and Exhibition; OnePetro: Moscow, Russia, 2006.
(18) Hashemi, A.; Nicolas, L. M.; Gringarten, A. C. Well-Test Analysis of Horizontal Wells in Gas/Condensate Reservoirs. *SPE Reservoir Eval. Eng.* **2006**, *9*, 86−99.
(19) Al-Baqawi, A. M.; Al-Malki, B. H. *Well Test Analysis in Naturally Fractured Gas Condensate Reservoirs Below Dew Point Pressure*, Asia Pacific Oil and Gas Conference & Exhibition; OnePetro: Jakarta, Indonesia, 2009.
(20) Cao, L. N.; Li, X. P.; Luo, C.; et al. Horizontal well transient rate decline analysis in low permeability gas reservoirs employing an orthogonal transformationmethod. *J. Nat. Gas Sci. Eng.* **2016**, *33*, 703−716, DOI: 10.1016/j.jngse.2016.06.001.
(21) Muskat, M. *Physical Principles of Oil Production*; McGraw-Hill Book Company Inc.: 1949.
(22) Jones, J. R.; Raghavan, R. Interpretation of flowing well responsein gas condensate wells. *SPE Form. Eval.* **1988**, *3*, 578−574, DOI: 10.2118/14204-pa.
(23) Jones, J. R.; Raghavan, R. Interpretation of Pressure Buildup Reservoirsin Gas Condensate Well. *SPE From. Eval.* **1989**, *4*, 93−104, DOI: 10.2118/15535-PA.
(24) Fevang, Ø.; Whiston, C. H. Modeling gas-condensate well deliver-ability. *SPE Reservoir Eng.* **1996**, *11* (4), 221−230, DOI: 10.2118/30714-pa.
(25) Gringarten, A. C.; AI-Lamki, A.; Daungkaew, S.et al.*Well Test Analysis in Gas-Condensate Reservoirs*, Proceedings of SPE Annual Technical Conference and Exhibition; OnePetro, 2000.
(26) Gringarten, A.; Bozorgzadeh, M.; Hashemi, A.et al. *Well Test Analysis in Lean Gas Condensate Reservoirs: Theory and Practice*, SPE Russian Oil and Gas Technical Conference and Exhibition; OnePetro, 2006.
(27) Zhang, W.; Cui, Y.; Jiang, R. Z.; et al. Production performance analysis for horizontal wells in gas condensate reservoir using three-

https://doi.org/10.1021/acsomega.3c10360
ACS Omega 2024, 9, 17307−17322

region model. *J. Nat. Gas Sci. Eng.* **2018**, *61*, 226−236, DOI: 10.1016/j.jngse.2018.11.004.
(28) Li, J.; Zhao, G.; Jia, X.; et al. Integrated study of gas condensate reservoir characterization through pressure transient analysis. *J. Nat. Gas Sci. Eng.* **2017**, *46*, 160−171, DOI: 10.1016/j.jngse.2017.07.017.
(29) Dastan, A.; Kamal, M. M.; Hwang, Y.et al. *Falloff Testing Under Multiphase Flow Conditions in Naturally Fractured Reservoirs*, SPE Western Regional Meeting; OnePetro, 2018.
(30) Dahim, S.; Taghavinejad, A.; Razghandi, M.; et al. Pressure and rate transient modeling of multi fractured horizontal wells in shale gas condensate reservoirs[J]. *J. Pet. Sci. Eng.* **2020**, *185*, No. 106566.
(31) Wang, Y.; Cheng, S.; Zhang, K.; et al. Investigation on the Transient Pressure Response of Water Injector Coupling the Dynamic Flow Behaviors in the Wellbore, Waterflood−Induced Fracture and Reservoir: SemiAnalytical Modeling and A Field Case. *Int. J. Heat Mass Transfer* **2019**, *130*, 668−679, DOI: 10.1016/j.ijheatmasstransfer.2018.09.083.
(32) Wei, C.; Liu, Y.; Cheng, S.; et al. Temperature Transient Analysis of Naturally Fractured Geothermal Reservoirs. *SPE J.* **2022**, *27*, 12723−2745, DOI: 10.2118/205862-PA.
(33) Yin, F. G.; Cheng, S. Q.; Liu, X.; et al. Semianalytical Modeling for Multiphase Flow in a Fractured Low-Permeability Gas Condensate Reservoir. *ACS Omega* **2023**, *8*, 32892−32906, DOI: 10.1021/acsomega.3c04183.
(34) Computer Modeling Group (CMG). *IMEX User Manual, MYR2017 Version*, 2017.
(35) Saleh, A. M.; Stewart, G. *Interpretation of Gas Condensate Well Tests With Field Examples*, SPE Annual Technical Conference and Exhibition; OnePetro: Washington, D.C, 1992.
(36) Duangkaew, S.; Ross, F.; Gringarten, A. C. *Well Test Analysis of Condensate Drop-Out Behavior in a North Sea len gas condensate reservoir*, SPE Annual Technical Conference and Exhibition; OnePetro, 2002.
(37) Warren, J. E.; Root, P. J. The behaviorofnaturally fractured reservoirs. *Soc. Pet. Eng.* **1963**, *3* (3), 245−255.
(38) Van Everdingen, A. F.; Hurst, W. The Application of the Laplace Transformation to Flow Problems in Reservoirs. *J. Pet. Technol.* **1949**, *1*, 305−324.
(39) Stehfest, H. Algorithm 368: Numerical inversion of Laplace transforms [D5]. *Commun. ACM* **1970**, *13* (1), 47−49.
(40) Pedrosa, O. A. *Pressure Transient Response in Stress-Sensitive Formations*, SPE California Regional Meeting; OnePetro: Oakland, California, 1986.
(41) Kikani, J.; Pedrosa, O. A. Perturbation Analysis of Stress-Sensitive Reservoirs. *SPE Form. Eval.* **1991**, *6*, No. 379, DOI: 10.2118/20053-PA.
(42) Guo, J.; Wang, H.; Zhang, L.; et al. Pressure transient Analysis and flux distribution for Multistage fractured horizontal wells in triple-porosity reservoir media with consideration of stress-sensitivity effect. *J. Chem.* **2015**, *2015* (1), No. 212901, DOI: 10.1155/2015/212901.
(43) Wang, H. T.; Guo, J. J.; Zhang, L. H. A semi-analytical model for multilateral horizontal wells in low-permeability naturally fractured reservoirs. *J. Pet. Sci. Eng.* **2017**, *149*, 564−578.
(44) Kong, X. Y. *Advanced Mechanics of Fluids in Porous Media*, 2nd ed.; University of Science and Technology of China Press, 2010.

https://doi.org/10.1021/acsomega.3c10360
ACS Omega 2024, 9, 17307−17322